aerospace

MDPI

Article

Optimization of Hole Geometry for Hot Air Anti-Icing Performance on Rotating Spinners

Wenhao Deng [1,2], Lingcheng Wang [1], Yuhang Li [3], Zhaoqi Liu [4], Tianyu Han [1], Borong Qiu [1], Yakang Xia [1], Haiwang Li [1,2] and Xuan Gao [1,2,*]

[1] Research Institute of Aero-Engine, Beihang University, Beijing 100191, China; dengwh@buaa.edu.cn (W.D.); wanglingcheng@buaa.edu.cn (L.W.); tianyuhan@buaa.edu.cn (T.H.); borongqiu@buaa.edu.cn (B.Q.); yakang_xia@buaa.edu.cn (Y.X.); lihaiwang@buaa.edu.cn (H.L.)
[2] Taihang National Laboratory, Chengdu 610213, China
[3] National Key Laboratory of Spacecraft Thermal Control, Beijing Institute of Spacecraft System Engineering, Beijing 100094, China; lyhlyhlyh88@126.com
[4] Contemporary Amperex Technology Co., Ltd. (CATL), Ningde 352100, China; lzqsqza@163.com
* Correspondence: xuangao@buaa.edu.cn

Abstract

Optimizing hole geometry for rotating hot air anti-icing spinners is computationally expensive and requires balancing overall icing suppression against extreme local ice thickness risk. This study proposes an integrated framework combining an $L_9(3^4)$ orthogonal design, multi-physics simulations, a dual-branch neural-network surrogate, and Pareto-based multi-objective optimization. Row spacing, column spacing, and hole diameter were jointly optimized. Across nine configurations, the area-averaged film heating effectiveness ranged from 0.108 to 0.5988, while the maximum ice thickness reached 3.16 mm. The surrogate simultaneously predicted pointwise ice thickness and film heating effectiveness, achieving R^2 values of 0.9751 and 0.8839, respectively. Minimizing maximum ice thickness and maximizing area-averaged film heating effectiveness revealed their trade-off, with the Pareto knee point yielding 0.863 mm and 0.451, respectively. The recommended configuration had a row spacing of 4.7187 mm, column spacing of 22.7646 mm, and hole diameter of 2.0639 mm. Validation under six icing conditions showed that maximum ice thickness decreased by 22.37–100% in the four baseline icing cases, and area-averaged film heating effectiveness increased by 54.45–68.01%, while compressor heat loss decreased by 12.2–16.6%. The proposed framework therefore provides an efficient method for rotating spinner anti-icing design.

Keywords: orthogonal experimental design; dual-branch coupled neural network; pareto-based multi-objective optimization; hot air anti-icing; rotating spinners

Check for updates

Academic Editor: Konstantinos Kontis

Received: 12 August 2026
Revised: 10 September 2026
Accepted: 29 September 2026
Published: 9 October 2026

Copyright: © 2026 by the authors. Licensee MDPI, Basel, Switzerland. This article is an open access article distributed under the terms and conditions of the Creative Commons Attribution (CC BY) license.

1. Introduction

During flight, an aircraft may pass through clouds. If the clouds contain a large number of supercooled water droplets, ice accretion will occur on the forward-facing surfaces of the aero-engine when they impinge on these surfaces [1,2]. In recent years, flight accidents caused by aero-engine icing have resulted in numerous casualties and significant economic losses. Common types of ice accretion include glaze ice, rime ice, and mixed ice. Glaze ice is hard and transparent, and its formation is often accompanied by the generation of runback water [3]. Rime ice, due to the entrainment of a large amount of air, is relatively soft [4]. Mixed ice is an ice morphology between these two types [5]. Common

aero-engine icing surfaces include stationary components such as the inlet [6], struts [7], guide vanes [8], and lip [9]. Rotating icing surfaces include the rotating spinner [5], fan blades [10], and low-pressure compressor blades [11]. Ice accretion on these components can lead to reduced intake airflow, inlet distortion, and even surge [12]. Once ice sheds and enters the aero-engine interior, it may damage the blades, causing engine failure [13].

Hot air anti-icing is a common method for aero-engine rotating spinners [14]. This method extracts hot air from the compressor, which flows through the internal disk cavity structure and is delivered to the bottom of the spinner. The hot air impinges on the inner surface of the spinner to achieve heating, thereby reducing ice accretion on the spinner surface. If holes are opened on the spinner surface, the hot air flowing out through these holes forms a hot air film on the surface, further enhancing the anti-icing effect. The hot air discharged from the holes flows back into the compressor together with the incoming flow; therefore, this method does not reduce the intake airflow and only incurs a small amount of heat loss [15]. In the design of the hole configuration for the hot air anti-icing spinner, the severity of ice accretion varies under different icing environments and aero-engine operating conditions. The same anti-icing design may perform well under mild icing conditions but may become less effective under severe icing conditions. Therefore, it is necessary to optimize the hot air anti-icing design scheme [16]. The parameters available for optimization of the hot air anti-icing rotating spinner include the blowing ratio, hole shape, hole inclination angle, hole arrangement, and number of holes. If each parameter takes five values, the total number of hot air anti-icing spinner configurations formed by all parameter combinations is 3125. Performing modeling, meshing, and ice accretion calculations for each of these 3125 configurations individually, followed by comparison of their anti-icing performance, would incur an unacceptable time cost [17]. Therefore, it is necessary to develop a tool capable of rapidly predicting ice accretion.

Artificial neural networks (ANNs) have been increasingly applied to icing prediction because they can approximate nonlinear mappings between operating conditions and icing responses at substantially lower cost than repeated experiments or numerical simulations. Early research focused primarily on reproducing ice shapes on stationary two-dimensional airfoils. Conformal mapping, Fourier-series representation, and a feedforward neural network were combined to predict ice geometry from atmospheric and flight conditions [18]. Although the method reproduced rime ice reasonably well, it was restricted to single-valued ice shapes and interpolation within the training range. Wavelet packet transform was subsequently introduced to compress ice-shape information, and BP, RBF, and generalized regression networks were compared for predicting NACA0012 ice shapes [19]. However, airfoil geometry, angle of attack, and three-dimensional surface icing were not included and required further investigation.

More recently, a geometrical constraint-enhanced neural network was developed by incorporating ice shape fluctuation constraints into the loss function [20]. This approach improved the smoothness and accuracy of icing thickness predictions for a two-dimensional NACA0012 airfoil. Nevertheless, the training samples covered a limited range of geometric and operating conditions, and the model did not consider rotating components or anti-icing heat-transfer performance. A BP network was also embedded in a Monte Carlo Lagrangian droplet solver to predict droplet impingement probability, reducing the computational cost of three-dimensional airfoil and nacelle calculations [16]. However, the neural network accelerated only the droplet-collection stage and did not predict subsequent water-film evolution, phase change, ice thickness, or surface film heating effectiveness. Neural networks have also been applied to wind-turbine icing monitoring. BP and RBF networks were used to infer ice mass and location from changes in blade modal frequencies [21], while a deep neural network using SCADA variables was developed to identify the bi-

nary icing state of wind-turbine blades [22]. These studies demonstrated the potential of data-driven icing assessment, but their outputs were regional ice mass or icing status rather than spatially resolved ice-thickness and thermal-performance fields. Moreover, their models were not coupled with the physical processes governing aircraft hot air anti-icing. Taken together, existing neural-network icing studies mainly address isolated tasks such as two-dimensional ice-shape reconstruction, droplet-impingement acceleration, ice-mass estimation, or icing-state classification. These models generally use atmospheric or operational parameters as inputs and produce a single icing-related output. The coupled influence of film-hole row spacing, column spacing, and diameter on a rotating hot air anti-icing spinner has not been systematically represented together with the rotational-force model, thermal–fluid–structural coupled model, and phase interface data exchange model. A spatially resolved surrogate capable of simultaneously predicting surface ice thickness and film heating effectiveness is likewise absent, leaving a methodological gap in the efficient evaluation and optimization of rotating-spinner anti-icing configurations. Recent studies have further demonstrated the potential of machine learning for icing-related prediction. Kallarappayi et al. [23] compared ensemble and deep-learning models for wind turbine icing prediction over 1, 6, and 24 h horizons and showed that physically meaningful sensor and weather forecast inputs were more influential than model complexity. Cardona et al. [24] employed Decision Tree, Random Forest, and XGBoost models to predict aircraft anti-icing fluid endurance using natural and artificial snow data, with the optimized XGBoost model achieving $R^2 = 0.92$. However, these methods mainly predict scalar icing probability or fluid endurance rather than spatially resolved ice thickness and thermal performance fields.

Many engineering design problems involve objectives that cannot be improved simultaneously. Pareto-based multi-objective optimization retains a set of non-dominated solutions instead of reducing competing objectives to a single weighted function, thereby allowing their trade-offs to be examined after optimization. A representative example is the multi-objective grey wolf optimizer, which uses an external archive to preserve Pareto-optimal solutions and guide population evolution [25]. Among evolutionary approaches, NSGA-II has become one of the most widely used methods because its fast non-dominated sorting, elitist preservation, and crowding-distance mechanism provide a practical balance between convergence and solution diversity [26]. Its broad applicability has been demonstrated in problems such as cloud-computing task scheduling, where completion time and load balance are optimized simultaneously [27], and multimodal route planning, where travel time, cost, and discomfort are treated as competing objectives [28]. These studies confirm the ability of Pareto-based methods to reveal compromises among conflicting criteria, although the physical meaning of the objectives remains application-dependent. In aircraft hot air anti-icing design, a reduced-order optimization framework combining proper orthogonal decomposition, a radial-basis-function neural network, and NSGA-II was developed for a three-dimensional wing piccolo-tube system [15]. Five geometric variables describing the jet-hole spacing, piccolo-tube position, and jet angles were considered. The multi-objective problem maximized the average temperature within the protected region while minimizing the total runback-water mass flow rate, subject to constraints on bleed-air consumption and water outflow. The resulting Pareto front demonstrated a clear conflict: Increased evaporation reduced the remaining runback water but consumed more of the available heat, thereby lowering the average surface temperature. This work established the feasibility of surrogate-assisted multi-objective optimization for hot air anti-icing systems. Nevertheless, the existing objective formulation evaluates anti-icing performance mainly through surface temperature and runback-water flow, which are indirect thermal and hydrological indicators. Average temperature may conceal a localized

icing peak, whereas total runback-water flow does not directly quantify the ice that has already formed on the protected surface. Consequently, a design with acceptable global indicators may still contain a locally hazardous ice ridge. Conversely, minimizing only the maximum ice thickness may suppress the most severe local peak while redistributing ice over a broader surface region. The maximum surface ice thickness and a surface-averaged heating-effectiveness measure have not been jointly incorporated into a Pareto-based objective system. Existing studies therefore do not directly provide a set of alternative designs that balances control of the maximum ice thickness against reductions in local cumulative ice accretion, especially for a rotating hot air anti-icing spinner.

Whereas CFD-only approaches require repeated high-cost simulations, existing machine learning models mainly predict scalar icing states or fluid endurance, and previous anti-icing optimization studies generally use indirect temperature or runback water indicators. The present framework couples multi-physics CFD with a spatially resolved dual-output surrogate and Pareto optimization to directly balance maximum ice thickness and area-averaged film heating effectiveness through spinner film-hole geometry. In this study, an orthogonal experimental design is employed to jointly optimize the row spacing, column spacing, and hole diameter, and a coupled computational framework incorporating a rotational force model, a thermal–fluid–structural coupled model, and a phase interface data exchange model is established. The dual-branch coupled neural network is developed to simultaneously predict the ice thickness and film heating effectiveness over the spinner surface. In the multi-objective genetic algorithm, minimizing the maximum ice thickness and maximizing the area-averaged film heating effectiveness are formulated as two competing objectives to reveal the trade-off between extreme ice thickness risk and ice accretion amount. By comparing the anti-icing performance of the spinner before and after optimization, the effectiveness of the proposed optimization method and computational procedure is validated, providing a reference for the design and optimization of aero-engine hot air anti-icing systems.

2. Numerical Method

2.1. Model of Icing

In the anti-icing calculation of a rotating spinner with hot air anti-icing for aero-engines, it is typically necessary to compute the clean flow field, then calculate the droplet impingement process, and finally perform the ice accretion calculation. In the clean flow field calculation, the Spalart–Allmaras (S-A) turbulence model is applied to solve the Navier–Stokes equations [29], and a thermal–fluid–structural coupling method is adopted to generate the solid wall mesh for heat conduction calculation. The velocity–pressure coupling is solved using the Pressure Implicit with Splitting of Operators (PISO) algorithm.

In the droplet impingement calculation, the Eulerian method is applied to solve the droplet motion equations, with the centrifugal force and Coriolis force coupled into the droplet motion. The entire solution process is established in a rotating coordinate system. The droplet dynamic motion equation is as follows [30]:

$$\frac{\partial(\rho\alpha)}{\partial t} + \nabla\cdot\left(\rho\alpha\vec{v}_r\right) = 0 \tag{1}$$

$$\frac{\partial\left(\rho\alpha\vec{v}_r\right)}{\partial t} + \nabla\cdot\left(\rho\alpha\vec{v}_r\otimes\vec{v}_r\right) + \rho\alpha\left[2\vec{\omega}\times\vec{v}_r + \vec{\omega}\times\left(\vec{\omega}\times\vec{r}\right)\right] = \rho\alpha K\left(\vec{v}_a - \vec{v}_r\right) \tag{2}$$

where ρ is the droplet density, α is the water volume fraction, $\vec{v}_{\mathrm{r}}$ is the droplet velocity vector, $\vec{\omega}$ is the rotating velocity vector, $\vec{r}$ is the radius vector, and $\vec{v}_{\mathrm{a}}$ is the air velocity vector. K is the air-water droplet exchange coefficient.

In the hot air anti-icing method of this study, hot air is extracted from the root of the first-stage rotor blade of the compressor, flows through the internal disk cavity structure, and is delivered to the bottom of the spinner. The hot air then flows out through the film holes on the spinner wall, forming a hot air film on the surface. The bleed air process and the ice accretion mechanism are illustrated in Figure 1. This method is based on the VOF approach [31,32], incorporating a rotational force model and a phase-interface data exchange model, and it has undergone comprehensive model development and icing wind tunnel validation [5]. Hot air not only forms a hot air film on the outer surface but also impinges on the inner wall for heating, creating a coupled internal–external hot air anti-icing effect. In summary, the ice accretion process of supercooled water droplets on a hot air anti-icing spinner is a complex, coupled multiphase heat and mass transfer flow process.

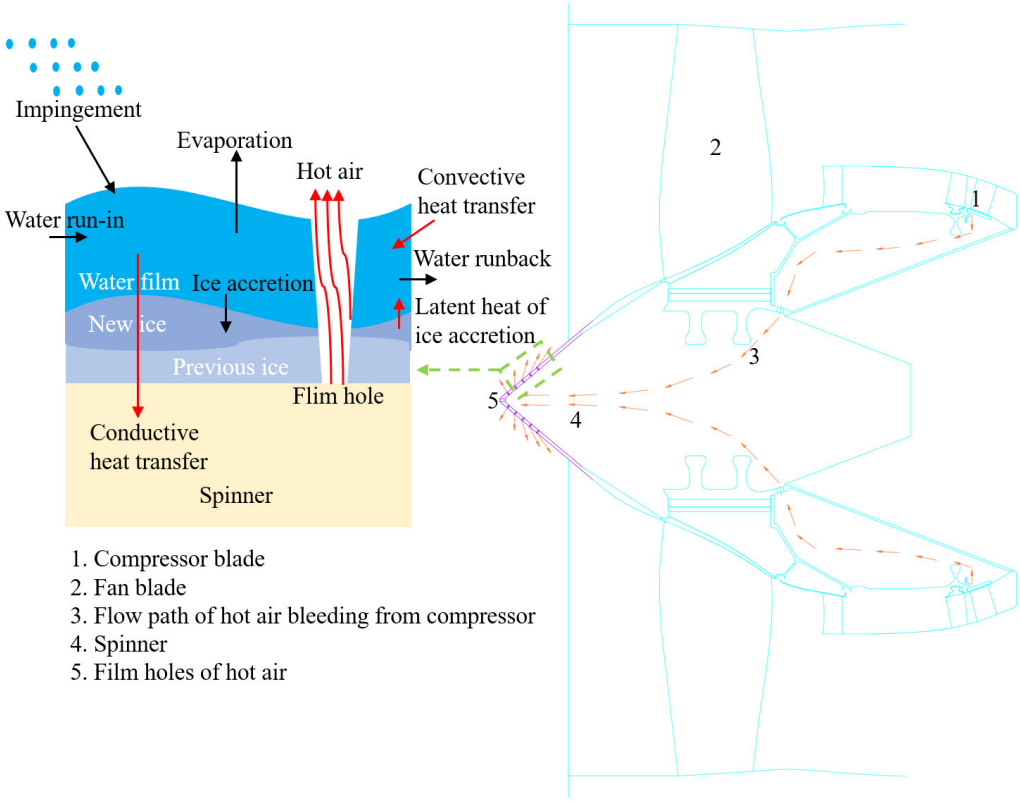

Figure 1. Bleeding air flow path and heat transfer mechanisms of the hot air anti-icing process.

The mass variation during the icing process can be described by the following mass balance equation:

$$\Delta \dot{m} = \dot{m}_{flow} + \dot{m}_{imp} - \dot{m}_{evapo} - \dot{m}_{ice} \tag{3}$$

where $\Delta \dot{m}$ is the water source term, $\dot{m}_{flow}$ is the water film flowing mass flow rate between control volumes, $\dot{m}_{imp}$ is the mass flow rate of impingement, $\dot{m}_{evapo}$ is the mass flow rate of evaporation, and $\dot{m}_{ice}$ is the reduced water mass flow rate due to icing.

The energy variation during the icing process can be described by the following energy balance equation:

$$\dot{Q}_{\text{evapo}} + \dot{Q}_{\text{ice}} + \dot{Q}_{\text{conv}} + \dot{Q}_{\text{cond}} = \Delta E_{water} + \Delta E_{ice} \tag{4}$$

where $\dot{Q}_{\text{evapo}}$ is the latent heat associated with evaporation, $\dot{Q}_{\text{ice}}$ is the latent heat released during icing, $\dot{Q}_{\text{conv}}$ is the convective heat transfer, $\dot{Q}_{\text{cond}}$ is the conductive heat transfer, and ΔE_{water} and ΔE_{ice} represent the changes in the internal energy of water and ice.

The phase-interface data exchange model [33] is used to describe the temperature gradient and water film flow within the control volume, and its heat conduction balance equation is as follows:

$$\kappa_{\text{ice}} \times \frac{0 - T_{\text{ice}}}{m_{ice}^{'}/\rho_{\text{ice}}} = \kappa_{\text{water}} \times \frac{T_{\text{new}} - 0}{m_{water}^{'}/\rho_{\text{water}}} \tag{5}$$

where κ_{ice} and κ_{water} are the thermal conductivity of ice and water, T_{ice} and T_{new} are the temperatures of the new ice and water film at the new time step, $m_{ice}^{'}$ and $m_{water}^{'}$ are the masses of ice and water at the new time step, and ρ_{ice} and ρ_{water} are the densities of the ice and water film.

In the rotational force model [5], the spinner is assumed to be stationary, and the centrifugal force $\vec{F}_s$, Coriolis force $\vec{F}_a$, and shear force due to rotating air $\vec{F}_r$ are introduced into the VOF momentum equation in the form of momentum source terms to describe the rotation process of the spinner, as shown below:

$$-\nabla p + \nabla \cdot \left[\mu \left(\nabla \vec{v} + \nabla \vec{v}^{T} \right) \right] + \rho \vec{g} + \vec{F}_s + \vec{F}_r + \vec{F}_a = \frac{\partial}{\partial t} \left(\rho \vec{v} \right) + \nabla \cdot \left(\rho \vec{v} \vec{v} \right) \tag{6}$$

When studying the thermal load on a rotating spinner with film heating, determining the near-wall hot film temperature (T_{f}), also known as the heat exchange temperature, is essential. Since film heating involves the mixing of the cold incoming flow and hot air, T_{f} depends on both the incoming flow temperature T_{in} and the hot air temperature T_{h}. To characterize this relationship, a dimensionless temperature η denoting film heating effectiveness is introduced to replace T_{f} [34]:

$$\eta = \frac{T_f - T_{in}}{T_h - T_{in}} \tag{7}$$

The theoretical maximum value of η is 1, indicating $T_{\text{f}} = T_h$, meaning that the hot air completely covers the spinner surface and the incoming cold air has no effect on the spinner surface temperature. η can be less than 0, which occurs when the hot air outlet velocity is relatively high. The total temperature at the hot air inlet is constant. When the hot air outlet velocity is high, a substantial portion of the internal energy of the hot air is converted into kinetic energy, resulting in a reduction in the internal energy of the hot air. Consequently, T_{f} may fall below the incoming flow temperature. According to the definition of η, $\eta < 0$ in this case.

2.2. Neural Network Surrogate Model and Multi-Objective Optimization

Before constructing the surrogate model, the geometric sample set was generated using a three-factor, three-level $L_9(3^4)$ orthogonal design. Orthogonal arrays provide balanced coverage of the factor space with substantially fewer runs than a full factorial design [35]. The pairwise balance condition of the array is expressed as

$$\text{D} = L_9(3^4) \in \{1,2,3\}^{9\times 4} \tag{8}$$

$$\text{N}_{\text{jk}}(\text{a,b}) \equiv \text{card}\{\text{i:D}_{\text{ij}} = \text{a,D}_{\text{ik}} = \text{b}\} = 1,\ \text{j} \neq \text{k},\ \text{j,k} \in \{1,2,3,4\},\ \text{a,b} \in \{1,2,3\} \tag{9}$$

where D is the 9 by 4 level-index matrix of the $L_9(3^4)$ orthogonal array; i denotes the configuration number; j and k denote two different design factors; and a and b denote their level indices. The cardinality operator counts the number of configurations containing a specified pair of levels. A value of one means that every level pair for any two factors occurs exactly once, while each individual level occurs three times in each column. In this

study, the three factors were the row spacing A, column spacing B, and hole diameter C. A, B, and C occupy the first three columns, while the fourth column is left empty to preserve the structure of the orthogonal array. Therefore, j and k denote two different columns of the orthogonal array rather than necessarily two physical design factors. Consequently, nine representative spinner configurations were simulated instead of all 27 combinations of the full factorial design.

Although only nine independent configurations were simulated, the L_9 orthogonal array provides balanced and efficient coverage of the three-factor, three-level design space. Each factor level appears three times, and every pair of factor levels occurs once, thereby reducing factor correlation and maximizing the information obtained from a limited number of costly CFD simulations. The three levels of each factor allow the design to represent nonlinear trends, while the balanced pairwise combinations provide information on combined parameter effects. Nevertheless, nine independent configurations cannot fully resolve higher-order interactions, densely represent the three-dimensional response surface, or exclude unsampled local optima. Although the large number of surface points improves the learning of spatial distributions, it does not increase the number of independent geometric configurations. To mitigate these limitations, the data were divided by complete configuration, the network was selected using an independent validation configuration, and dropout, L_2 regularization, and batch normalization were applied. The optimization was restricted to the sampled parameter ranges, and the resulting Pareto solutions were regarded as surrogate-based candidate optima rather than guaranteed global optima. The selected knee-point configuration was subsequently re-evaluated using full CFD simulations under six icing conditions, confirming its improvement over the baseline design. Therefore, the present surrogate is intended for interpolation within the investigated design space, while future work will introduce additional space-filling or adaptively selected configurations, particularly near the predicted Pareto front, to better quantify nonlinear interactions and assess the robustness of the identified optimum.

A coupled neural network surrogate model was developed to replace repeated high-cost CFD evaluations during optimization of the spinner hole configuration. The dataset was divided by complete spinner configuration rather than by randomly sampling individual surface points. Spinners 1, 2, 4, 6, 7, 8, and 9 were used for training, Spinner 3 for validation, and Spinner 5 for independent testing. This configuration-level partition prevented spatially adjacent points from the same spinner from appearing in different subsets, thereby reducing information leakage. Wide, deep, and dual-branch candidate networks were trained under identical conditions. The dual-branch architecture was selected using the validation set, while the independent test case was used only to assess generalization.

For surface point i, the model input combines the three hole-configuration parameters and the local Cartesian coordinates. Equation (10) is an application-specific input definition of the present study, consistent with recent CFD-oriented neural-network surrogate formulations that map parameter vectors and local descriptors to engineering responses [36]:

$$x_{\mathrm{i}} = \left[p^{\mathrm{T}}, r_{\mathrm{i}}^{\mathrm{T}}\right]^{\mathrm{T}} = [\mathrm{A}, \mathrm{B}, \mathrm{C}, x_{\mathrm{i}}, y_{\mathrm{i}}, z_{\mathrm{i}}]^{\mathrm{T}} \tag{10}$$

A, B, and C are the hole row spacing, column spacing, and hole diameter. x_{i}, y_{i}, and z_{i} are the Cartesian coordinates of surface point i. The two vectors therefore represent the structural parameters and local position. All inputs were standardized using training-set statistics. The validation and test sets use the same normalization parameters. Considering that the ice thickness contains a large number of near-zero values and exhibits a significantly skewed distribution, the inverse hyperbolic sine function is first applied:

$$h^{*} = \operatorname{asinh}\left(\frac{h}{10^{-4}}\right) \tag{11}$$

It is transformed and then normalized. The dimensionless η is directly normalized. After prediction, inverse normalization and inverse transformation are applied to the two outputs, and any negative ice thickness values that may occur are corrected to zero.

Following recent multi-input and multi-response neural network surrogate formulations for engineering design [37,38], the selected network processes the structural parameters and spatial coordinates through two separate feature-extraction branches and then fuses the extracted features to predict the local ice thickness and film heating effectiveness:

$$\hat{y}_i = F_f\left(\left[F_p\left(\tilde{p}\right); F_r\left(\tilde{r}_i\right)\right]; \theta\right), \hat{y}_i = \left[\hat{H}_{ice,i}, \hat{\eta}_i\right]^T \tag{12}$$

where $\hat{y}_i$ denotes the predicted output vector at surface point i. The two branch operators in Equation (12) extract structural and coordinate features, and the fusion operator maps the concatenated features to local ice thickness and film heating effectiveness. The structural branch contains 128 and 64 neurons, the coordinate branch contains 256 and 128 neurons, and the fusion network contains 256, 128, 64, and 32 neurons. Fully connected layers use batch normalization and ReLU activation, with a dropout rate of 0.1 in the fusion network.

The network parameters were determined by minimizing the regularized multi-output mean squared error, with L2 weight decay used to limit overfitting and improve generalization, as adopted in neural network surrogate studies [36,37]:

$$L(\theta) = E_{i \in D_{tr}}\left[\left(\tilde{y}_i - \hat{\tilde{y}}_i\right)^T\left(\tilde{y}_i - \hat{\tilde{y}}_i\right)\right] + \lambda\theta^T\theta \tag{13}$$

where the expectation is evaluated over the training set; $\left(\tilde{y}_i - \hat{\tilde{y}}_i\right)^T\left(\tilde{y}_i - \hat{\tilde{y}}_i\right)$ is the standardized reference and predicted outputs; θ contains the trainable parameters; and λ is the L2 regularization coefficient. Adam optimization and a fixed 60-epoch schedule were used. After the independent-test assessment, the selected dual-branch network was retrained with all nine configurations to produce the final coupled model. Separately trained ice thickness and film heating effectiveness networks were retained for cross-checking.

The final surrogate model was then embedded in the multi-objective optimization framework. For each candidate design, the coupled model predicted both responses over the optimization surface set. The two objectives were defined as

$$\min_p F(p) = [H_{ice,max}(p), -\eta_{ave}(p)]^T \tag{14}$$

$$H_{ice,max} = \max_{i \in \Omega_{opt}} \hat{H}_{ice,i}, \eta_{ave} = \sum_{i \in \Omega_{opt}} \frac{\hat{\eta}_i A_{c,i}}{\sum A_{c,i}} \tag{15}$$

where the first objective is the maximum predicted ice thickness H_{ice} over the optimization surface, and the second is the negative area-averaged value of the predicted film heating effectiveness η, and A_c is the base area of the spinner surface mesh. These two objective definitions are specific to the present anti-icing problem. The latter form converts efficiency maximization into minimization. Predictions outside the physical efficiency interval were penalized rather than clipped. The Pareto set was generated by MATLAB gamultiobj (MATLAB R2023a), a controlled elitist multi-objective genetic algorithm and variant of NSGA-II [39], using 48 individuals, 60 generations, and a Pareto fraction of 0.5.

The valid Pareto set provided a minimum ice solution, a maximum effectiveness solution, and a compromise knee-point solution. The representative knee point was selected

using the normalized Euclidean distance to the ideal point, consistent with the recent distance-to-ideal criterion for identifying a balanced Pareto solution [40]:

$$\mathrm{p}_{\mathrm{knee}} = \underset{\mathrm{p}\in\mathcal{P}}{\operatorname{argmin}} \sqrt{\overline{H}^2(\mathrm{p}) + \overline{E}^2(\mathrm{p})} \tag{16}$$

where the calligraphic set $\mathcal{P}$ denotes the valid Pareto solutions, while $\overline{\boldsymbol{H}}(\mathrm{p})$ and $\overline{\boldsymbol{E}}(\mathrm{p})$ denote the normalized deviations of the maximum ice thickness and area-averaged film heating effectiveness from their respective ideal values. The three representative designs were re-evaluated over the full spinner surface, cross-checked using the independent surrogate models, and examined by parameter-sensitivity analysis. Finally, the recommended hole configuration was reconstructed and verified by an additional CFD simulation.

2.3. Simulation Procedure

The overall framework of the hole-configuration optimization and validation procedure is illustrated in Figure 2 and consists of four main modules.

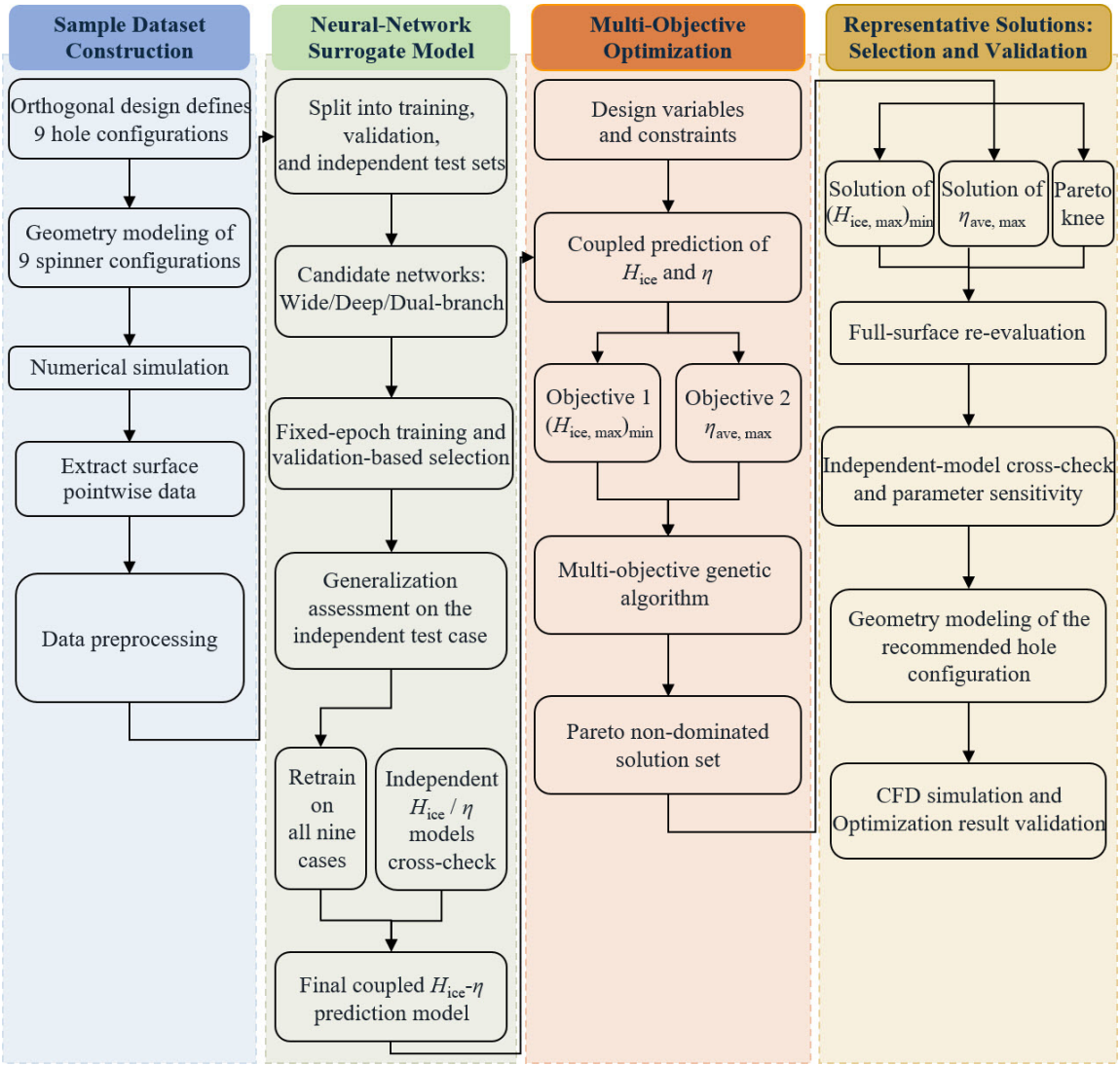

Figure 2. Overall framework for neural-network-assisted multi-objective optimization and validation of the film-hole configuration for rotating hot air anti-icing spinners.

(1) Sample Dataset Construction. An orthogonal design ($L_9(3^4)$) was employed to define nine representative hole configurations. The corresponding spinner geometries were constructed and numerically simulated, after which the pointwise surface data were extracted and pre-processed.

(2) Neural Network Surrogate Model. The dataset was divided into training, validation, and independent test sets. Wide, deep, and dual-branch networks were trained and compared, and the selected network was assessed using the independent test case. It was subsequently retrained using all nine configurations to obtain the final coupled H_{ice}-η prediction model.

(3) Multi-Objective Optimization. Within the prescribed design variable ranges and constraints, the coupled surrogate model was used to predict the maximum H_{ice} and average η. A multi-objective genetic algorithm was then applied to minimize $(H_{ice})_{max}$ and maximize η_{ave}, producing a Pareto non-dominated solution set.

(4) Representative Solutions: Selection and Validation. The minimum $(H_{ice})_{max}$ solution, maximum η_{ave} solution, and Pareto knee-point solution were selected and re-evaluated over the full spinner surface. After independent-model cross-checking and parameter-sensitivity analysis, the recommended hole configuration was reconstructed and validated through an additional CFD simulation.

3. Results and Discussion

3.1. Model and Computational Setup Based on Orthogonal Experimental Design

In traditional hot air anti-icing film-hole structural design, the optimization primarily relies on engineering experience and enumeration methods, repeatedly adjusting the film-hole structural parameters and performing CFD calculations to find the optimal configuration. This approach is labor-intensive, inefficient, and unable to traverse all possible combinations of film-hole parameters. With the development of artificial intelligence optimization algorithms, design methods combining CFD and optimization algorithms have gradually become a research hotspot. Such combined approaches can rapidly construct ice accretion prediction models and efficiently search for optima through optimization algorithms. This study proposes an intelligent optimization scheme for film-hole parameters based on orthogonal experimental design, a neural network fast prediction model, and a multi-objective optimization algorithm. Orthogonal experimental design can scientifically select highly representative parameter combinations with the fewest number of experiments, ensuring uniformity and comparability of data in the parameter space. The optimization of hot air anti-icing hole parameters conducted in this study was validated solely through numerical simulation. Experimental validation of the optimized spinner has been included in future research plans.

In the orthogonal experimental design, the row spacing A (mm), column spacing B (mm), and hole diameter C (mm) are selected as the three optimization parameters. The definition of these parameters is shown in Figure 3a. It should be noted that the leading-edge hole diameter is 6 mm and is treated as a fixed parameter in this study. Based on engineering experience, combined with the geometric constraints of the hot air anti-icing rotating spinner and the anti-icing requirements, the value ranges of the three parameters are determined as follows: A: 4–12 mm; B: 20–40 mm; C: 1–3 mm. Three levels are uniformly selected within the range of each parameter for the experiments: A = 4, 8, 12 mm; B = 20, 30, 40 mm; C = 1, 2, 3 mm. According to the factors and number of levels of this experiment and the required degrees of freedom, the $L_9(3^4)$ orthogonal array is chosen for the experimental design. The $L_9(3^4)$ orthogonal array contains nine experiments, can accommodate four factors with three levels each, and has a total degree of freedom of eight. This orthogonal array fully meets the requirements, with a small number of experiments and the highest

computational efficiency. The orthogonal design table of film-hole parameters is shown in Table 1. In the table, the spinner number represents the film-hole parameters of the spinner under nine different parameter combinations. A, B, and C correspond to the three columns of the orthogonal array. Spinner 3 was used for validation and model selection, whereas Spinner 5 was kept completely unseen during training and model development and was evaluated only once after the network architecture had been selected. Hole structure generally includes hole shape, arrangement pattern, hole count, etc. Since different hole shapes are difficult to parameterize, only the hole diameter was selected as an optimization parameter. Once the row spacing and column spacing of the holes are determined, the hole count is also fixed. Therefore, under the premise of a uniform hole arrangement, the optimization of the hole count is not studied separately.

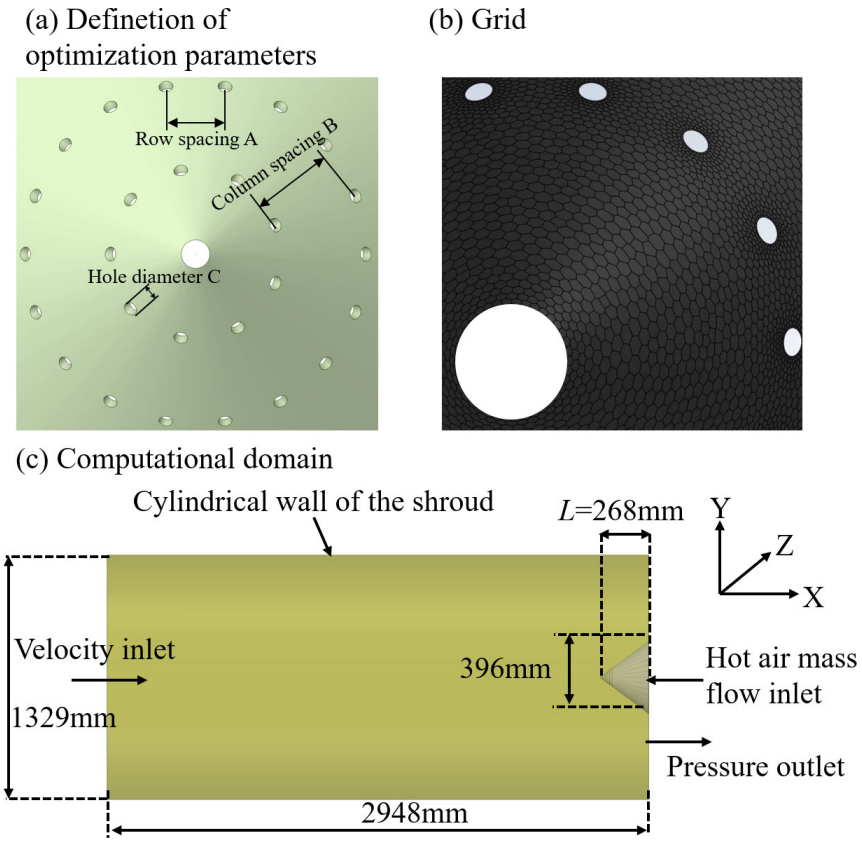

Figure 3. Definition of optimization parameters, surface grid details, and computational domain.

Table 1. Orthogonal experimental design table of film-hole parameters (A1 = 8 mm, A2 = 4 mm, A3 = 12 mm; B1 = 30 mm, B2 = 20 mm, B3 = 40 mm; C1 = 2 mm, C2 = 1 mm, and C3 = 3 mm).

Spinner Number	Row Spacing A	Column Spacing B	Hole Diameter C	Empty Column
1	A1	B1	C1	–
2	A1	B2	C2	–
3	A1	B3	C3	–
4	A2	B1	C2	–
5	A2	B2	C3	–
6	A2	B3	C1	–
7	A3	B1	C3	–
8	A3	B2	C1	–
9	A3	B3	C2	–

Nine groups of spinner configurations corresponding to the orthogonal array were modeled, as shown in Figure 4. Different film-hole parameters correspond to different spinner configurations, requiring separate modeling, meshing, and simulation calculations.

Since the modeling methods and computational procedures for the nine spinner configurations are essentially the same, only Spinner 1 is introduced here as an example. The surface mesh details of Spinner 1 are shown in Figure 3b. The total number of cells is 5.88 million, the minimum cell size near the spinner wall is 0.1 mm, and the near-wall y^+ is 4, satisfying the requirement of $y^+ < 30$ for the S-A turbulence model. The computational domain of the hot air anti-icing spinner was established, as shown in Figure 3c. The computational domain is a cylinder with a radius of 1329 mm and a length of 2948 mm. The spinner base has a diameter of 396 mm, a length of 268 mm (L), and a spinner half-cone angle of 37°. The leading-edge hole diameter on the spinner is 6 mm. For the sidewall holes, the row spacing A is 8 mm, the column spacing B is 30 mm, and the hole diameter C is 2 mm. The following boundary conditions are applied to the computational domain: velocity inlet, pressure outlet, hot air mass flow inlet at the spinner base, coupled heat transfer boundary condition on the spinner wall, and adiabatic boundary condition on the cylinder surface. Based on the icing wind tunnel test results, the aero-engine idle mixed-phase icing condition, which yields the most severe ice accretion, is selected as the baseline condition for the calculation. The inlet pressure is 101,325 Pa, the inlet velocity is 38 m/s, the inlet temperature T_{in} is −10 °C, and the outlet pressure is 100,047 Pa. The spinner rotational speed ω is 1800 rpm, the hot air inlet temperature is 3 °C, the hot air mass flow rate is 0.0489 kg/s, and the hot air inlet pressure is 93,000 Pa. The liquid water content LWC is 2 g/m^3, the median volumetric diameter MVD is 20 μm, and the icing duration is 300 s. A grid independence study was performed. The area-averaged film heating effectiveness η of the spinner was calculated for grids with total cell counts of 2.18 million, 3.83 million, 5.88 million, and 8.13 million. The results are shown in Table 2. Compared with the circumferentially averaged η obtained from the 8.13 million cell grid, the circumferentially averaged η error of the 2.18 million cell grid is 2.9%, and the error of the 3.83 million cell grid is 1.96%, while that of the 5.88 million cell grid is 0.32%. The error of the 5.88 million cell grid selected in this study is significantly smaller than that of the 2.18 million cell grid and the 3.83 million cell grid, and the computational error introduced by the grid is within an acceptable range.

Table 2. Grid independence validation of circumferentially averaged η.

X/L	η (2.18 million)	η (3.83 million)	η (5.88 million)	η (8.13 million)
0.0932	0.261555	0.208265	0.244547	0.241872
0.1032	0.220914	0.21807	0.228149	0.228648
0.1234	0.246143	0.246598	0.240259	0.239781
0.1828	0.291442	0.292238	0.283501	0.282002
0.5457	0.219529	0.215834	0.212082	0.212361
error	2.9%	1.96%	0.32%	Baseline 0%

The selected 5.88 million cell grid therefore showed an observed mesh sensitivity of 0.32% for the selected quantity of interest. In addition, the relative discrepancy between the predicted and measured maximum ice thickness remained below 10% for this method [5]. These results support the predicted overall ice-covered regions and comparative trends under the investigated conditions. However, a full probabilistic propagation of the input uncertainties was not performed, and uncertainties associated with local ice morphology, ice shedding, and other unresolved physical processes remain.

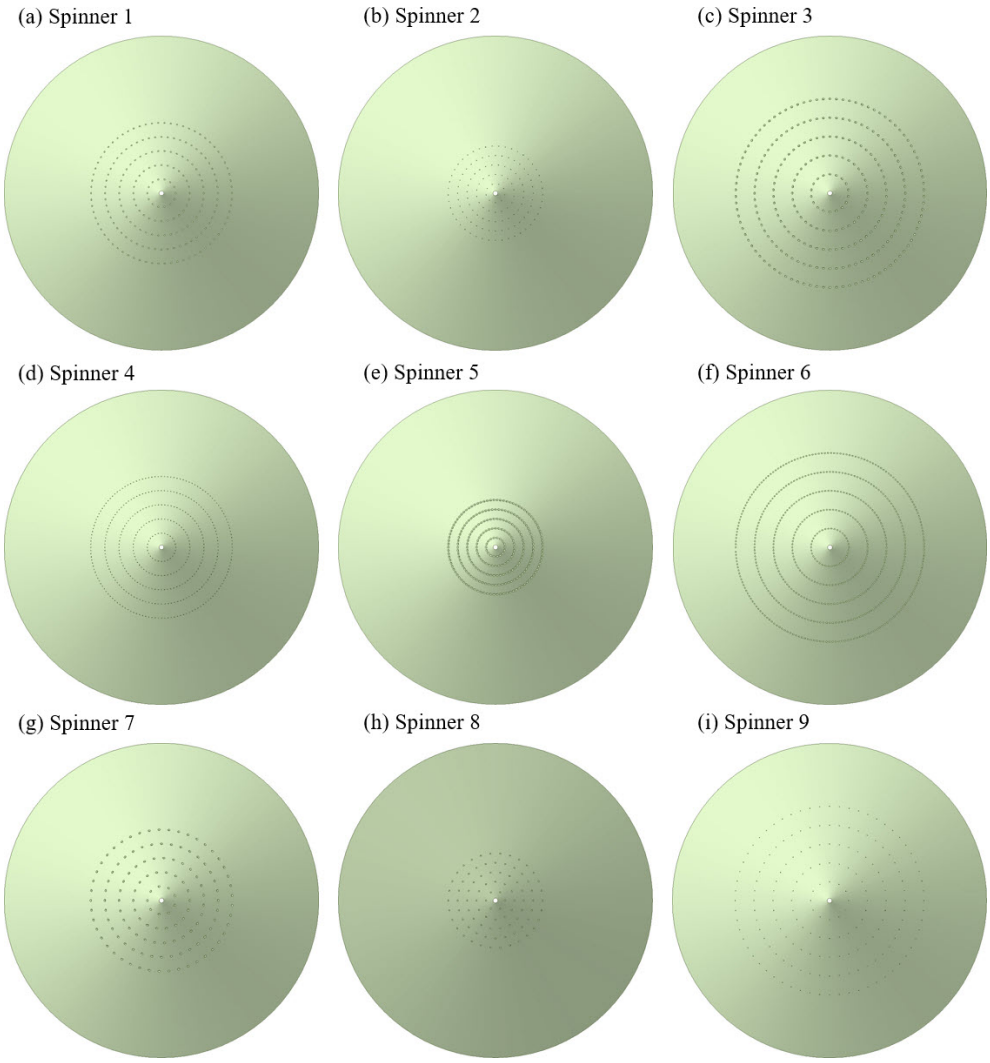

Figure 4. Models of the orthogonal experimental designed spinners.

3.2. Anti-Icing Performance of the Designed Spinners

Unlike conventional single-parameter studies, the present work jointly varies the row spacing, column spacing, and hole diameter to support their coordinated optimization. The numerical evaluation combines the rotational force model, thermal–fluid–structural coupled model, and phase interface data exchange model introduced in Section 2.1. The resulting η, β (local water collection efficiency), and H_{ice} fields therefore reflect the combined effects of spinner rotation, hot air heating, droplet impingement, wall conduction, and ice accretion.

Numerical simulations were performed on the nine spinner configurations obtained from the orthogonal experimental design. Representative parameters from the clean flow field calculation, droplet impingement calculation, and ice accretion calculation (η, β, and H_{ice}) were selected to analyze the anti-icing performance of the orthogonal experimental spinner configurations. The surface film coverage of the hot air anti-icing spinner is an important indicator for evaluating anti-icing effectiveness. Using the dimensionless temperature parameter η to represent the temperature distribution on the spinner surface can effectively describe the mixing degree of the surface film. η distributions of the nine spinner configurations are shown in Figure 5. For ease of comparison, the ranges of η_{min} and η_{max} in each figure were unified, with η_{min} set to 0 and η_{max} set to 1. The η_{min}, η_{max}, and area-averaged film heating effectiveness η_{ave} of the nine spinner configurations are

listed in Table 3. For Spinners 2 and 9, η_{min} is less than 0. The excessively high exit velocity at the film-holes causes the local static temperature to be much lower than the total temperature. According to Equation (7), when T_f is lower than T_{in}, $\eta < 0$. On the surfaces of Spinners 2 and 9, the region where $\eta_{min} < 0$ accounts for only 0.97% of the total spinner surface area. Therefore, limiting the color bar range in Figure 5 to 0–1 does not affect the overall η distribution. The overall η values of Spinners 2 and 9 are relatively low, while those of Spinners 3, 5, and 6 are relatively high. Moreover, the overall η distribution of Spinner 3 exhibits a pronounced rotational flow pattern. The overall η distributions of Spinners 1, 4, 7, and 8 are moderate. From the η distributions of different configurations, it can be seen that the film-hole parameters have a significant influence on the η distribution. Spinner 3 has the largest η_{max} (0.9913), while Spinner 2 has the smallest η_{max} (0.6669). Spinner 1 has the largest η_{min} (0.1158), while Spinner 2 has the smallest η_{min} (−1.4436). Spinner 5 has the largest η_{ave} (0.5988), while Spinner 9 has the smallest η_{ave} (0.108). η is an evaluation parameter for surface film coverage and is strongly correlated with the surface heat transfer calculation. η_{ave} can accurately reflect the overall η distribution on the surface. In the ice accretion calculation (see Equations (3) and (4)), $\dot{Q}_{conv}$ directly affects $\dot{m}_{ice}$. Spearman's rank correlation coefficient ρ_{sr} of the local ice accretion amount is −0.641. This shows a strong correlation with $\dot{m}_{ice}$ and indirectly reflects the ice accretion amount on the spinner surface, making it an important evaluation parameter for hot air anti-icing; the relevant research conclusions have been subjected to detailed quantitative analysis, and validation of parameter correlations was carried out in another study [34].

Table 3. η_{max}, η_{min}, and η_{ave} of orthogonal designed spinners.

Spinner Number	η_{max}	η_{min}	η_{ave}
1	0.9321	0.1158	0.2653
2	0.6669	−1.4436	0.1662
3	0.9913	0.0389	0.3476
4	0.9065	0.0802	0.2771
5	0.977	0.0468	0.5988
6	0.9913	0.0456	0.525
7	0.9395	0.0509	0.2079
8	0.7895	0.1006	0.2026
9	0.7434	−0.9819	0.1080

In the droplet impingement calculation for the hot air anti-icing spinner, the rotational force model and the effect of the hot air flow were coupled, and the local water collection efficiency β of the nine orthogonally designed spinner configurations was obtained, as shown in Figure 6. β distributions of Spinners 1–4 exhibit circumferentially non-uniform yet regular patterns, indicating a noticeable disturbance from the hot air flow. β distributions of Spinners 5–9 are relatively similar, showing weaker influence from the hot air. β_{max} occurs near the second and third rows of film holes on Spinner 1, with a value of 0.2416. To further quantitatively analyze β distribution, the circumferentially averaged β distributions of the nine designed spinners are plotted, as shown in Figure 7. For ease of analysis, the circumferentially averaged β distributions of Spinners 1–4, which are more significantly affected by the hot air flow, are presented in Figure 7a, while those of Spinners 5–9, which are less affected, are presented in Figure 7b. Spinners 1–3 are most influenced by the fluctuation of the hot air flow, with their β distributions exhibiting large fluctuations and peaks corresponding to the film-hole locations. Among them, Spinner 1 has the largest peak value of 0.089. Although the β distribution of Spinner 3 is closer to that shown in Figure 7b, it is still considerably affected by the hot air flow. β distributions of Spinners 5–9 nearly coincide with each other, with notable fluctuations only near the film holes, indicating that

variations in the film-hole parameters of these spinners have little effect on β distributions. β_{max} values of Spinners 5–9 are close to 0.12.

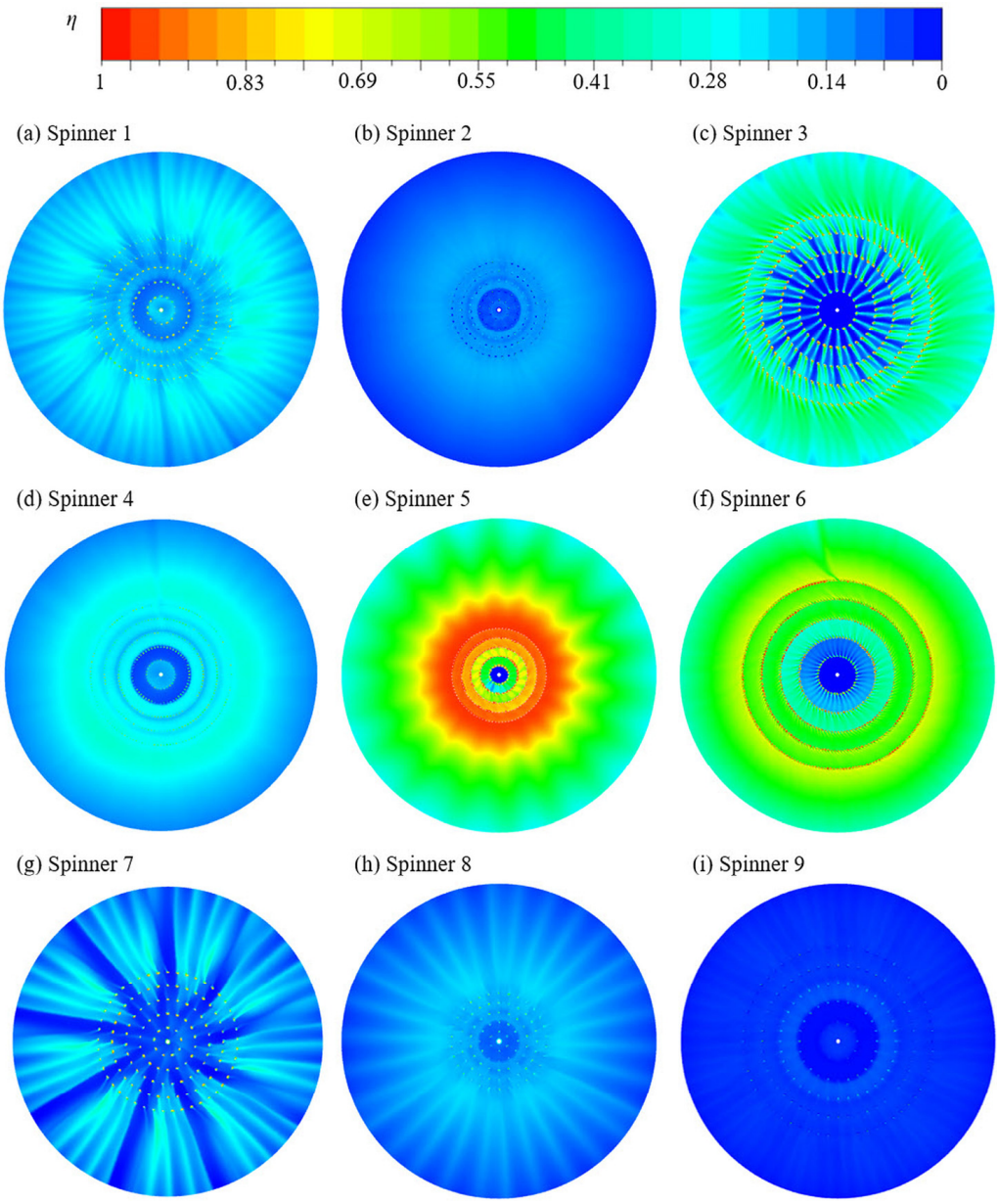

Figure 5. η distributions of 9 designed spinners.

Based on the clean flow field calculation results and droplet impingement calculation results from this section, the ice accretion model developed in Section 2.1 was applied to simulate the ice accretion of the nine orthogonally designed spinner configurations. The surface ice accretion height H_{ice} distributions of the nine spinners are shown in Figure 8. The ice accretion distribution is the result of the combined effects of multiple factors, including the incoming cold air, anti-icing hot air, spinner rotation, and droplet motion. It serves as a key parameter that directly reflects the hot air anti-icing performance. H_{ice} distributions vary considerably among Spinners 1–6. Spinners 3 and 6 are notably affected by the airflow, with their ice accretion distributions exhibiting strong rotational effects. H_{ice} distributions of Spinners 7–9 are relatively similar, and their overall coverage areas are the largest among the nine spinners. The maximum H_{ice} value occurs on Spinner 6, with a value of 3.16 mm. F_s on the rotating spinner gradually increases from the leading

edge to the trailing edge, and ice may shed due to F_s. In aero-engine anti-icing design, the earlier the ice shedding occurs and the smaller the shedding amount, the better the protective effect, because large ice shedding may damage the aero-engine blades and affect the safe and stable operation of the aero-engine. F_s at the spinner leading edge is very small, making ice shedding unlikely to occur. If H_{ice} at the leading edge is large, it poses a greater icing risk. The leading edges of Spinners 1, 2, and 4 are free of ice, indicating that these three configurations provide good protection for the leading edge.

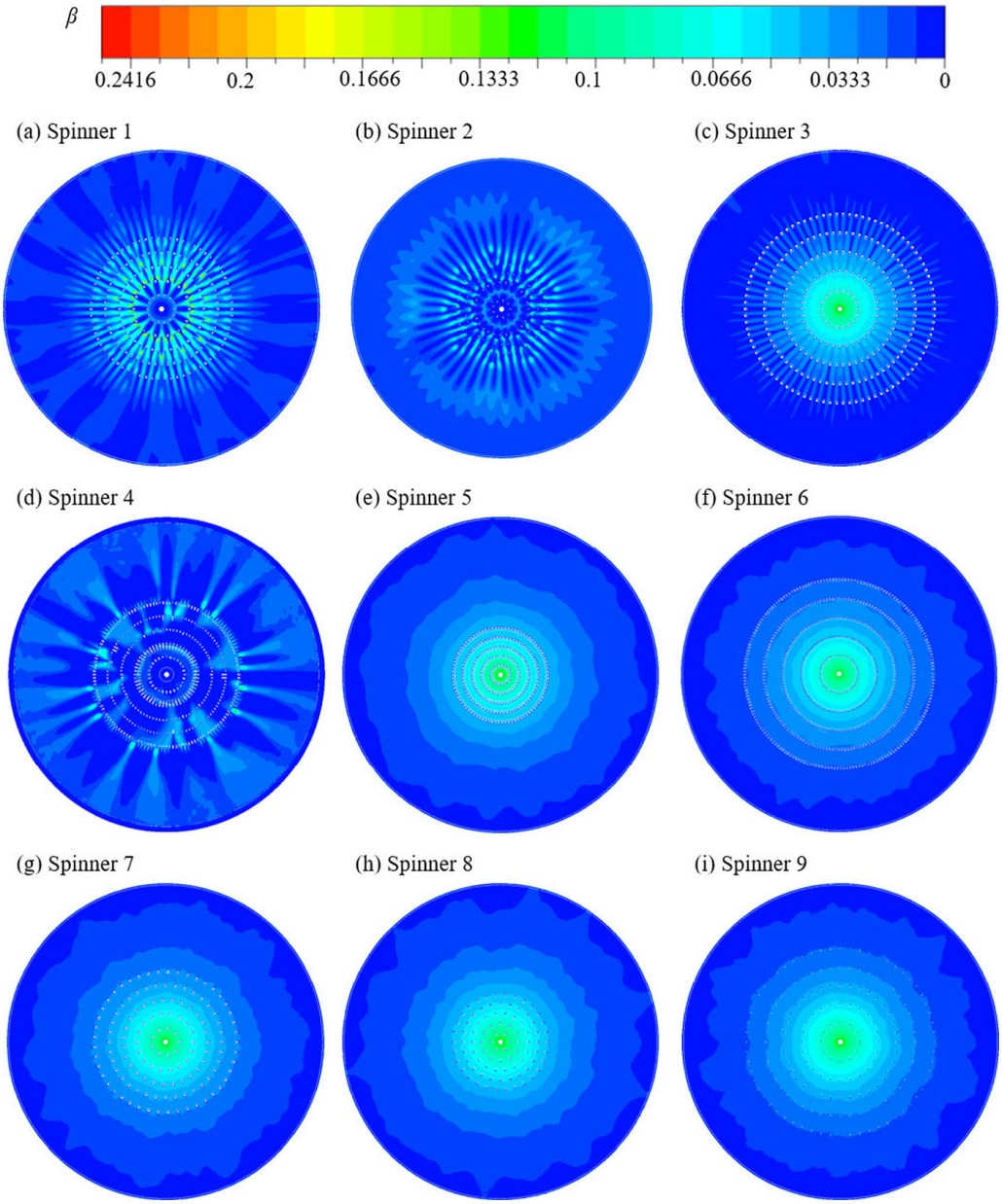

Figure 6. β distributions of 9 designed spinners.

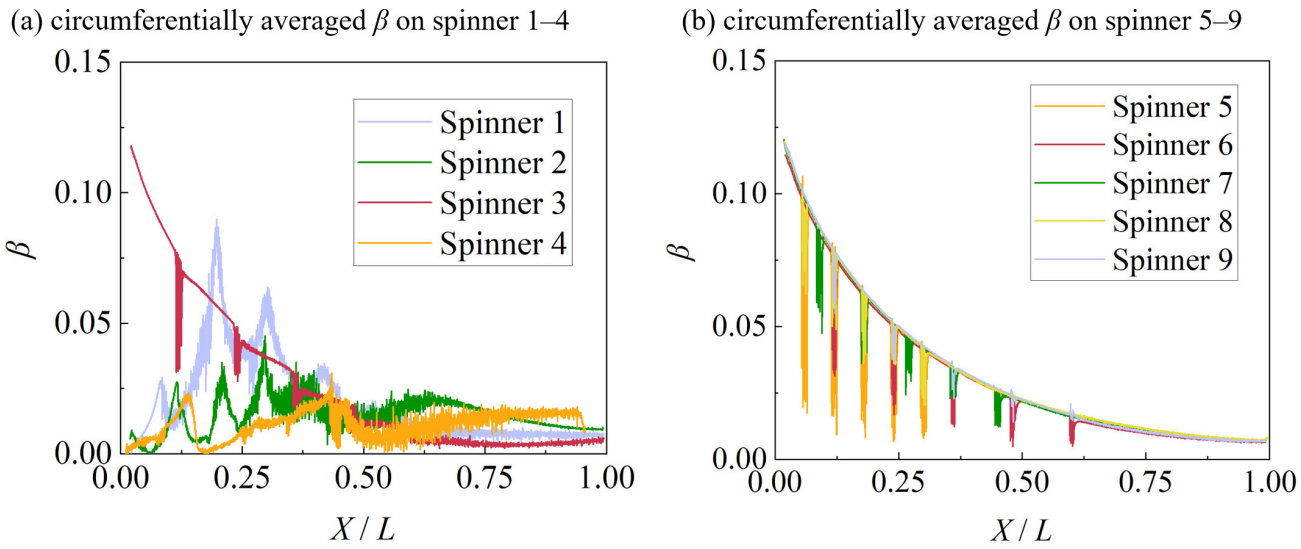

Figure 7. Circumferentially averaged β distributions of 9 designed spinners.

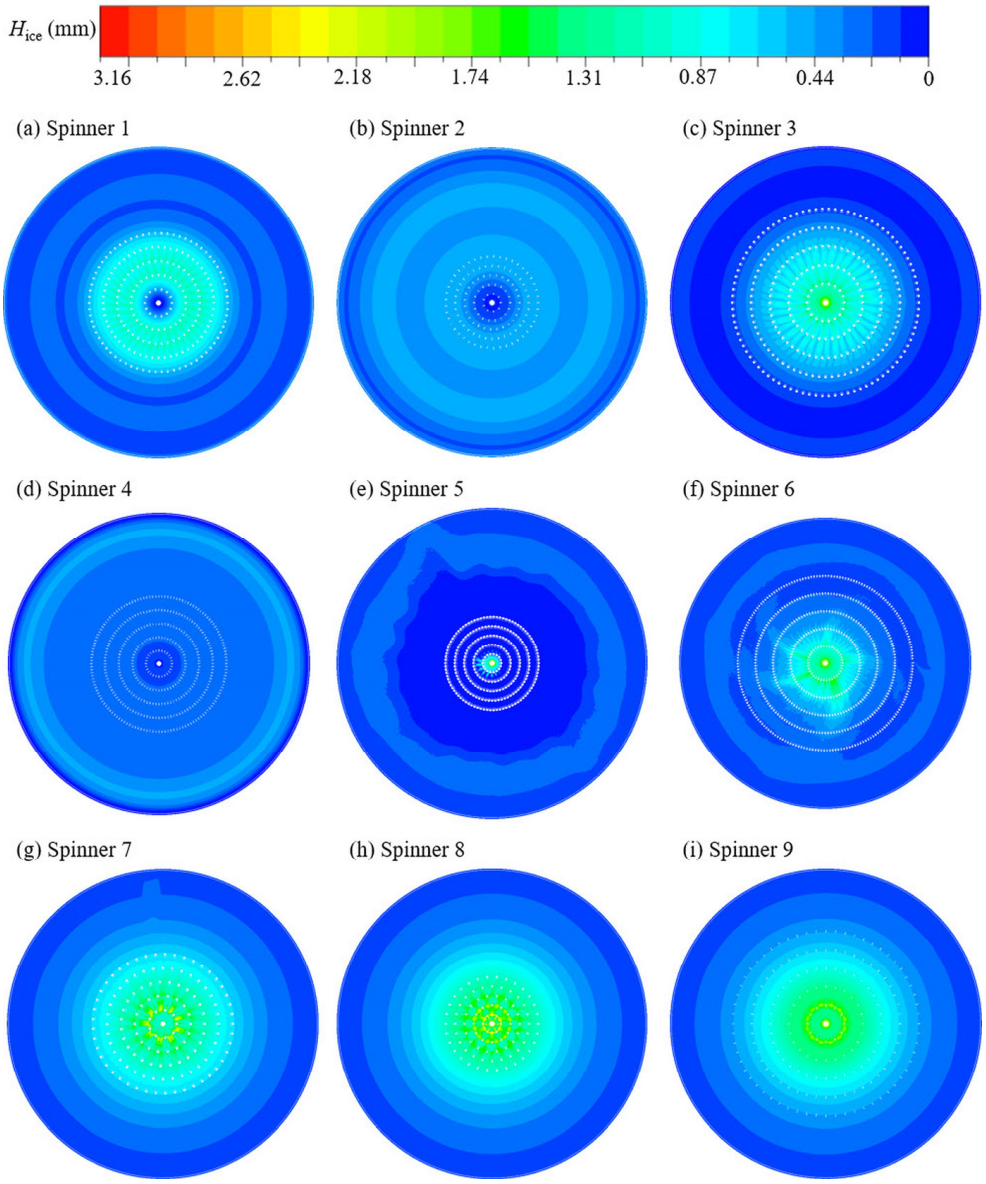

Figure 8. H_{ice} distributions of 9 designed spinners.

3.3. Prediction and Multi-Objective Optimization of Anti-Icing Performance

As discussed in Section 3.2, η and H_{ice} are both important parameters for evaluating anti-icing performance. η is negatively correlated with the amount of local ice accretion. It can characterize the overall icing level over the spinner surface, whereas H_{ice} directly describes local icing severity. Therefore, the pointwise η and H_{ice} were selected as the outputs of the neural-network surrogate model, and their surface statistics, η_{ave} and $H_{ice,max}$, were further used as the two objectives in the multi-objective optimization. This definition allows the optimization to consider both overall ice reduction and control of the most severe local icing region.

Figure 9 presents the training and validation histories of the selected dual-branch network during model selection. The validation loss reached its minimum at Epoch 3 and subsequently fluctuated without a sustained increase. The network weights corresponding to the minimum validation loss were retained, while dropout, L2 regularization, and batch normalization were employed to control overfitting. After model selection and independent testing, the selected architecture was retrained using all nine configurations to obtain the final coupled model used for optimization.

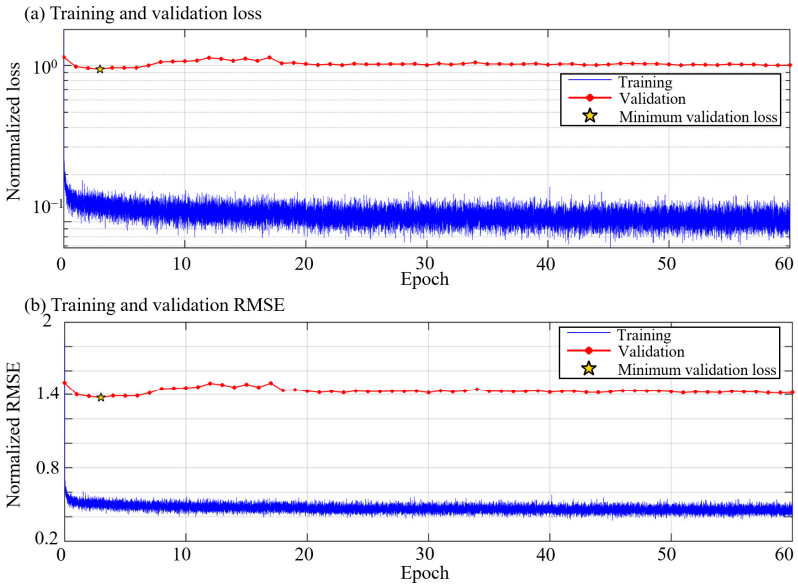

Figure 9. Training and validation loss and normalized RMSE histories of the dual-branch network during model selection.

The pointwise predictions of the final coupled network are compared with the numerical results used as reference data, as shown in Figure 10. For H_{ice}, most points are distributed close to the diagonal line, with R^2 = 0.9751 and an RMSE of 0.04623 mm. This agreement shows that the model captures both the magnitude and the main spatial variation of H_{ice} over the spinner surface. The largest H_{ice} values display slightly greater scatter and some underprediction, possibly because extreme samples are less numerous and local variation is sharper near severe icing regions. For η, the predicted and reference values also show a clear positive agreement, with R^2 = 0.8839 and an RMSE of 0.06688. The dispersion is greater than that for H_{ice}, particularly in the low η range, because only a small proportion of surface points falls within this interval. Despite the different response characteristics, the agreement for both outputs demonstrates the main advantage of the dual-branch coupled architecture: A single model can retain separate structural and spatial feature extraction while simultaneously predicting H_{ice} and η. This is important because the optimization algorithm must evaluate many candidate designs, while the remaining uncertainty can be examined through subsequent CFD validation.

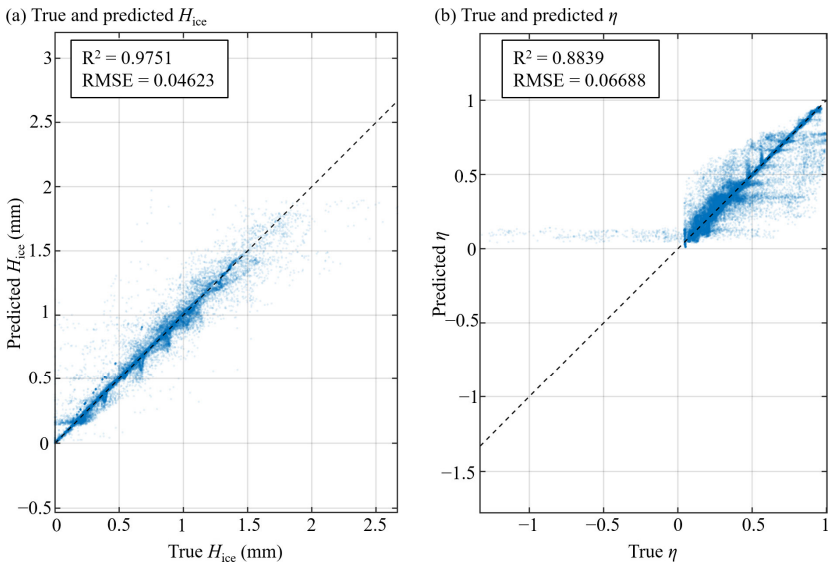

Figure 10. Prediction performance of the coupled neural network for H_{ice} and η.

Regarding hyperparameter configuration, a dual-branch coupled neural network was employed to process structural parameters and spatial coordinates separately. The structural branch takes the row spacing, column spacing, and hole diameter as inputs and contains 128 and 64 neurons. The coordinate branch takes the surface point coordinates x_i, y_i, and z_i as inputs and contains 256 and 128 neurons. After concatenating the features from the two branches, the fused features are passed through fusion layers containing 256, 128, 64, and 32 neurons, simultaneously outputting H_{ice} and η. Each fully connected module adopts batch normalization and the ReLU activation function, and a dropout layer with a dropout rate of 0.1 is placed after the first fusion layer. The network is trained using the Adam optimizer, with a maximum of 60 training epochs, a batch size of 8192, and an initial learning rate of 1.0×10^{-3}. The learning rate follows a piecewise decay strategy, multiplied by 0.3 every 20 epochs, resulting in learning rates of 1.0×10^{-3}, 3.0×10^{-4}, and 9.0×10^{-5} across the three training stages. Additionally, the gradient clipping threshold is set to 5, the L2 regularization coefficient is set to 2.0×10^{-5}, and the training samples are randomly shuffled at the beginning of each epoch. Data partitioning adopts a configuration-independent holdout strategy, where 3,999,351 surface points are used for training, 529,278 points from Configuration 3 are used for validation, and 516,787 points from Configuration 5 serve as the independent test set. Validation is performed approximately once per epoch. Wide networks, deep networks, and dual-branch networks are compared under identical training settings, and the model is selected based on the composite score of the normalized validation RMSE for both outputs. The dual-branch network achieves the lowest validation score, with the validation loss reaching its minimum at Epoch 3; therefore, the network weights corresponding to this epoch are retained. After model selection, the independent test configuration is evaluated only once for generalization capability. Subsequently, the selected network is retrained using all nine configurations to obtain the final model for multi-objective optimization. All RMSE and R^2 values are computed in terms of actual physical quantities after inverse transformation of the outputs. Training is performed on a CPU with a fixed random seed to ensure reproducibility.

In terms of overfitting control, after completing all 60 training epochs, the network parameters corresponding to the minimum validation loss are retained. Each epoch contains approximately 489 iterations, and the minimum validation loss occurs at the 1467th iteration (Epoch 3), where the validation loss and normalized validation RMSE are 0.9431 and 1.3734, respectively. After continuing training to Epoch 60, the training loss and training RMSE

decrease to 0.09990 and 0.44698, respectively; however, the validation loss and validation RMSE increase to 1.0037 and 1.4168, representing increases of approximately 6.43% and 3.16%, respectively, compared with the best validation point. This indicates that subsequent training further reduces the training error without improving validation performance, and the error gap between the training set and the validation set widens. Therefore, saving the model at the minimum validation loss mitigates the performance degradation caused by continued training; however, it cannot be concluded that overfitting has been completely avoided.

The trained coupled model was then embedded in the multi-objective genetic algorithm described in Sections 2.2 and 2.3. The nine orthogonal training configurations are compared with the Pareto-optimal candidates obtained by continuously searching the prescribed design space, as shown in Figure 11. The training configurations are located at the selected levels of A, B, and C and provide basic data for learning the parameter response relationship. In contrast, the Pareto candidates are concentrated within A = 4.45–5.10 mm, B = 20.71–23.12 mm, and C = 1.59–2.91 mm. The narrow ranges of A and B indicate that relatively small row and column spacings are generally preferred by the two objectives within the present constraints. Parameter C covers a wider interval and more clearly separates $(H_{ice,max})_{min}$, $(\eta_{ave})_{max}$, and knee-point solutions, showing that the hole diameter plays an important role in balancing the two objectives. Most Pareto candidates lie between rather than exactly at the nine original samples. This distribution demonstrates the interpolative role of the surrogate model: it enables the genetic algorithm to examine intermediate hole configurations without performing a new CFD simulation for every candidate.

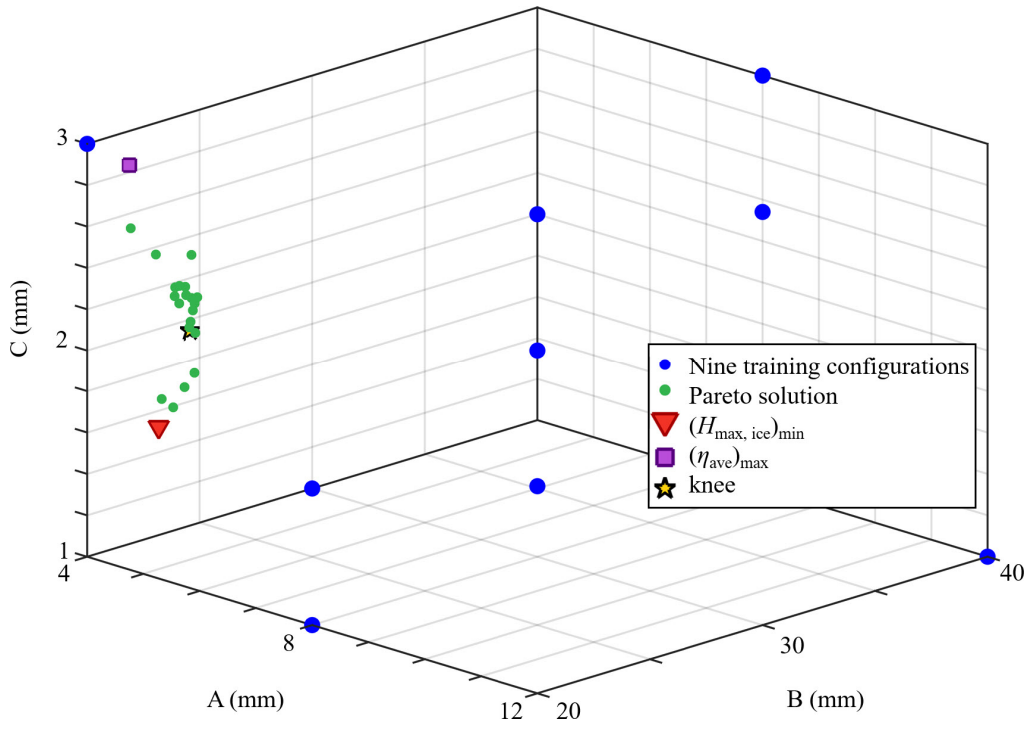

Figure 11. Distribution of training configurations and Pareto-optimal solutions in the hole parameter design space.

The Pareto front between $H_{ice,max}$ and η_{ave} is presented, as shown in Figure 12. As η_{ave} increases along the front, $H_{ice,max}$ also generally increases, confirming that the two objectives cannot be improved simultaneously over the current design range. The $(H_{ice,max})_{min}$ solution gives $H_{ice,max}$ = 0.382 mm and η_{ave} = 0.305, whereas the $(\eta_{ave})_{max}$ solution increases η_{ave} to 0.592 but also raises $H_{ice,max}$ to 1.994 mm. As discussed in Section 3.2, η_{ave}

is negatively correlated with the cumulative local icing amount over the surface, whereas $H_{ice,max}$ identifies the most severe local thickness. The opposing trend therefore reveals a direct trade-off: Reducing accumulated ice over the surface may concentrate the remaining ice within a limited region and increase the extreme H_{ice} risk. The knee-point solution, selected using the normalized distance criterion introduced in Section 2.2, lies between the two extremes, with $H_{ice,max}$ = 0.863 mm and η_{ave} = 0.451. Although it is not optimal for either individual objective, the knee-point solution provides a balanced compromise between them. Compared with the minimum H_{ice} solution, it increases η_{ave} from 0.305 to 0.451, while compared with the maximum η_{ave} solution, it reduces $H_{ice,max}$ from 1.994 to 0.863 mm. This balance is suitable for aero-engine hot air anti-icing because both overall surface heating and suppression of hazardous local ice accumulation must be considered. The color variation further shows that the hole diameter generally increases from the low H_{ice} end toward the high η end of the front. Thus, a larger diameter is associated with improved overall η, but it may also redistribute the surface heat load and increase $H_{ice,max}$. The knee-point solution was selected as the recommended anti-icing configuration for the spinner. The knee-point solution of hole parameters is as follows: A = 4.7187 mm, B = 22.7646 mm, and C = 2.0639 mm. The Pareto front therefore provides several feasible choices, allowing the final configuration to be selected according to the required balance between overall icing reduction and local icing risk. These surrogate model candidates are subjected to full surface re-evaluation and CFD validation below.

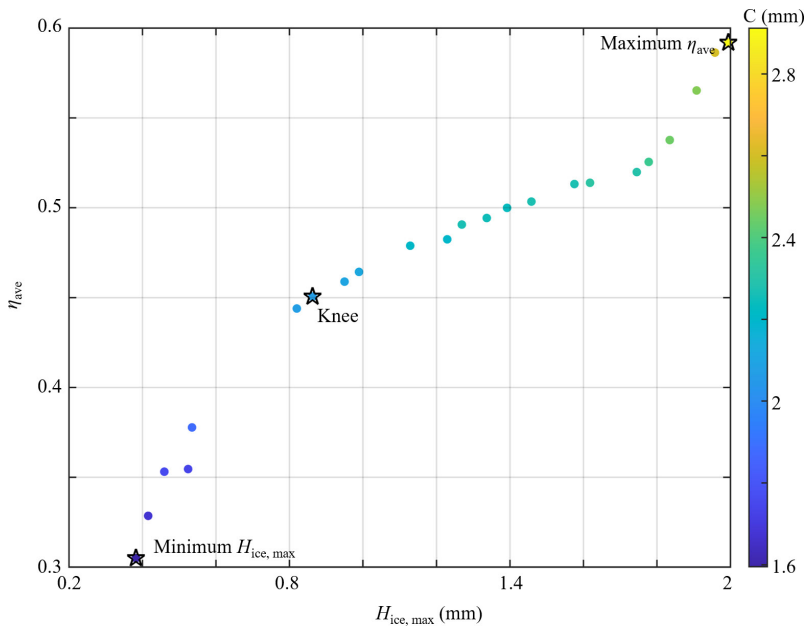

Figure 12. Pareto front and representative optimal solutions for H_{ice}, max and η_{ave}.

The Pareto front obtained in this study represents the nominal predictions of the neural-network surrogate rather than uncertainty-bounded solutions. Prediction errors in $H_{ice,max}$ and η_{ave} may shift individual Pareto points and the location of the knee point. Therefore, the selected knee-point design was treated as a candidate optimal configuration rather than a guaranteed global optimum. It was subsequently re-evaluated using full CFD simulations under six icing conditions. The CFD results showed reductions in $H_{ice,max}$ and increases in η_{ave} under the investigated conditions, confirming that the selected configuration provides an improvement over the baseline design. Nevertheless, quantitative epistemic uncertainty intervals and uncertainty-aware Pareto optimization require an ensemble of independently trained surrogate models or additional geometric configurations and remain subjects for future work.

Before performing the full CFD verification, the global sensitivity of the two objectives and the local robustness of the selected knee-point solution were further evaluated. A variance-based global sensitivity analysis was performed using the coupled surrogate model over the investigated design domain. A total of 512 base samples, corresponding to 4096 surrogate evaluations, were used to calculate the first-order, total-effect, and second-order Sobol indices. For $H_{ice,max}$, the total effect indices of C, B, and A were 0.632, 0.447, and 0.434, respectively, indicating that the hole diameter had the greatest overall influence. The relatively small first-order effect of A but appreciable total effect indicates that its influence was mainly introduced through parameter interactions. For η_{ave}, the total effect indices of A, C, and B were 0.77, 0.398, and 0.199, respectively, demonstrating that the row spacing was the dominant parameter. The A-C interaction was the strongest pairwise interaction for both $H_{ice,max}$ and η_{ave}, with second-order indices of 0.282 and 0.193, respectively.

The robustness of the selected Pareto knee point, [A,B,C] = [4.7187,22.7646,2.0639] mm, was further evaluated using 1024 samples with simultaneous ±5% perturbations of the three parameters. The resulting $H_{ice,max}$ had a mean of 0.9185 mm, a standard deviation of 0.1973 mm, and a 95% range of 0.5951–1.3384 mm. The corresponding η_{ave} had a mean of 0.4497, a standard deviation of 0.0234, and a 95% range of 0.4036–0.4925. Thus, η_{ave} remained relatively stable near the knee point, whereas $H_{ice,max}$ was more sensitive to geometric perturbations, particularly those involving the hole diameter and its interaction with the row spacing.

3.4. Anti-Icing Performance of the Optimized Spinner

The optimized hole parameters of the hot air anti-icing spinner are A = 4.7187 mm, B = 22.7646 mm, and C = 2.0639 mm. This spinner configuration was modeled and compared with the spinner configuration before optimization (A = 6.8 mm, B = 16.12 mm, and C = 2 mm), as shown in Figure 13. Compared with the spinner configuration before optimization, the optimized spinner features a larger film-hole coverage area. The row spacing of the holes is reduced, resulting in a higher hole distribution density. The hole diameter is increased, allowing more hot air to flow out through the sidewall holes. Based on the aero-engine operating conditions, six ice accretion calculation cases under idle and maximum states were defined, as listed in Table 4. Among them, Cases 1–3 correspond to the idle state, where the inflow velocity, temperature, and spinner rotational speed are low, and the hot air inlet mass flow rate and temperature are also low. Cases 4–6 correspond to the maximum state, where the inflow velocity, temperature, and spinner rotational speed are high, and the hot air inlet mass flow rate and temperature are also high. Cases 1 and 4 are glaze ice inlet boundary conditions. Cases 2 and 5 are mixed ice inlet boundary conditions. Cases 3 and 6 are rime ice inlet boundary conditions. Under idle conditions, the hot air inlet pressure (93,000 Pa) is lower than the freestream pressure (101,325 Pa). Nevertheless, the contracting internal geometry of the spinner and the suction effect near the holes accelerate the airflow, allowing the hot air inside the spinner to still be discharged through the holes without external cold air flowing into the spinner interior [41].

If full-process CFD calculations were adopted, assuming three variables A, B, and C, with intervals of 1 mm for A and B and 0.1 mm for C, a total of $9 \times 21 \times 21 = 3969$ sets of CFD calculations would be required. The CFD calculation consists of modeling and meshing (0.5 h), clean flow field calculations (3 h), droplet impingement calculations (1 h), and icing calculations (3 h), amounting to a total of $7.5 \times 3969 = 29{,}767.5$ h. The calculations were performed on a 60-core computer, consuming a total of 1,786,050 core-hours. If the optimization method in this study is adopted, nine sets of CFD calculations, neural network prediction, multi-objective optimization, and post-optimization CFD verification of the spinner are required, taking 68 h, 42 h, and 1 h, respectively, for a total of 111 h. The

calculations were performed on a 60-core computer, consuming a total of 6660 core-hours. Comparing the two approaches, the optimization method in this study saves 29,656.5 h (1236 days) in computational time and 1,779,390 core-hours in computational resources, a reduction of 99.63%. The comparison reveals that if traditional CFD were used, it would be impossible to perform full process icing calculations for all parameter combinations, as the resulting time and computational resource consumption would be unacceptable. Using the optimization method in this study, the time and computational resource consumption can be reduced by two orders of magnitude, and the optimized configuration has been validated through CFD calculations under multiple operating conditions, ensuring the reliability of the anti-icing performance optimization.

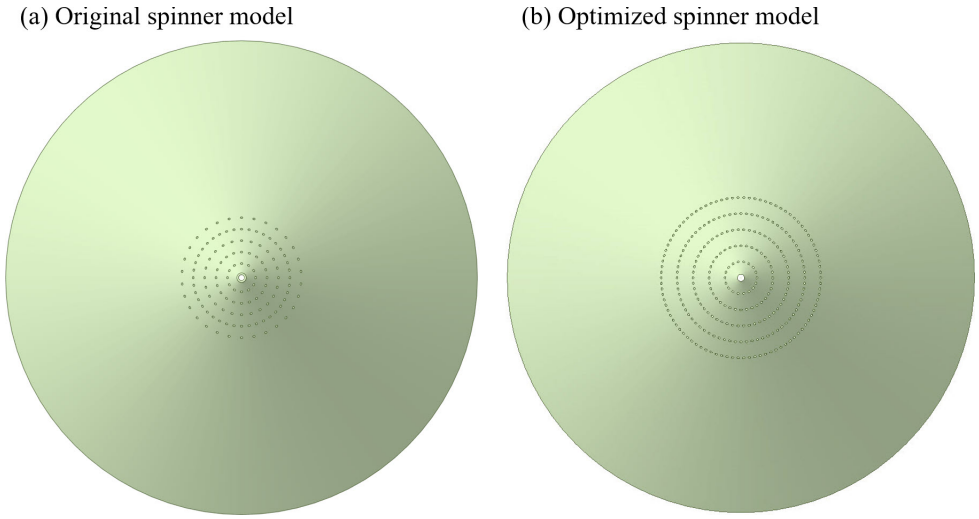

Figure 13. Models of original spinner and optimized spinner.

Table 4. Specification of the numerical icing conditions of optimized spinner.

Case	1	2	3	4	5	6
Operational state		Idle state			Maximum (Take-off) state	
Inlet pressure (Pa)	101,325	101,325	101,325	101,325	101,325	101,325
Outlet pressure (Pa)	100,049	100,047	100,049	79,695	79,066	79,059
Rotating velocity ω (rpm)	1800	1800	1800	6200	6200	6200
Inlet temperature T_{in} (°C)	−5	−10	−20	−5	−10	−20
Inlet velocity (m/s)	38	38	38	140	140	140
Hot air mass flow rate $\dot{m}_h$ (kg/s)	0.0489	0.0489	0.0489	0.195	0.195	0.195
Hot air temperature T_h (°C)	8	3	−8	69	63	27
Hot air total pressure (Pa)	93,000	93,000	93,000	180,000	180,000	180,000
LWC (g/m^3)	2	2	1	2	2	1
MVD (μm)	20	20	20	20	20	20
Icing time (s)	300	300	300	300	300	300

The clean flow field of the optimized hot air anti-icing spinner was calculated, and η distributions under Cases 1–6 were obtained, as shown in Figure 14. Cases 1–3 correspond to the idle condition, while Cases 4–6 correspond to the maximum condition. η distribution trends for the six cases are relatively similar: η values in the region of the first two rows of film holes are relatively low and begin to increase from the second row onward; when the hot air film develops to the trailing edge of the spinner, η decays to 0.22. Combining Figures 5 and 14, it can be observed that the η distribution is significantly influenced by the hole parameters of the spinner while being less affected by the boundary conditions. This indicates that the η distribution is primarily governed by the spinner structure.

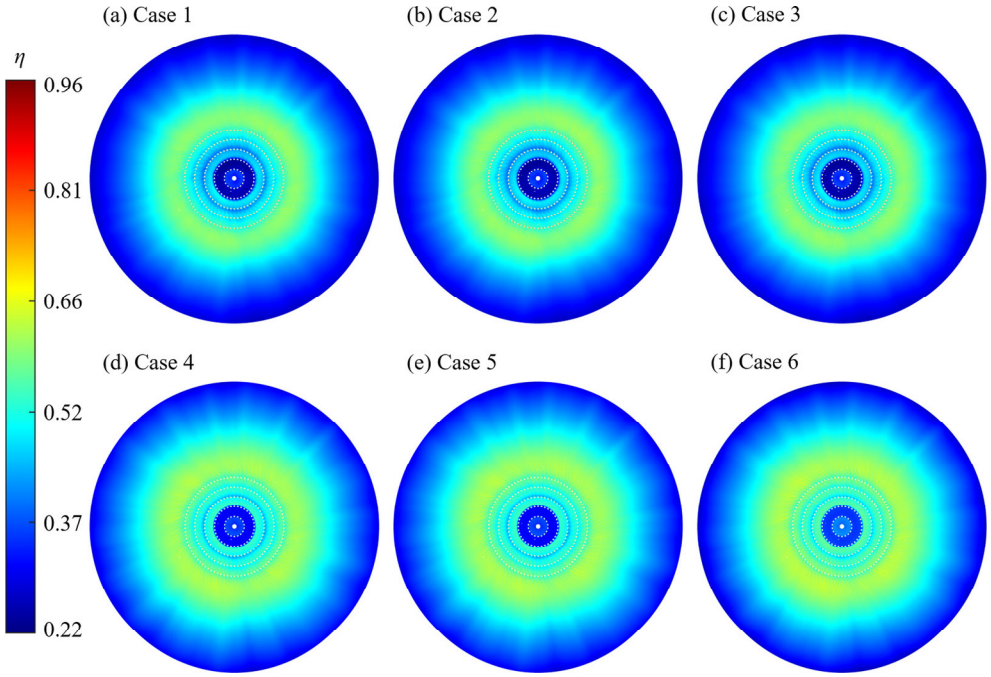

Figure 14. η distributions of the optimized spinner.

The ice accretion process of the optimized hot air anti-icing spinner was also calculated. The results show that Cases 1–3 experience ice accretion, while Cases 4–6 remain ice-free. H_{ice} distributions for Cases 1–3 are shown in Figure 15a, and the T_w distributions for Cases 4–6 are shown in Figure 15b. Case 1 exhibits only a small amount of ice accretion with low H_{ice} near the trailing edge of the spinner (see Figure 15(a1)). Under the idle glaze ice condition, the incoming flow temperature is relatively high, and the hot air temperature is also higher than that of Cases 2 and 3, resulting in an extremely small amount of ice accretion. The ice accretion in Cases 2 and 3 covers the entire spinner surface (see Figure 15(a2,a3), but no ice is present upstream of the first row of film holes. $H_{ice,max}$ for Cases 1–3 are 0.59 mm, 1.23 mm, and 0.81 mm, respectively. The surface T_w for Cases 4–6 are all above 0 °C, indicating that none of these three cases experience ice accretion.

Hot air anti-icing consumes compressor power, resulting in a compressor heat loss Q_{loss}. After the hot air flows from the compressor to the spinner surface, heat dissipates. The temperature difference ΔT_c from the compressor bleed point to the spinner outlet is the key parameter for calculating Q_{loss}. Q_{loss} can be calculated using the following equation:

$$Q_{loss} = \dot{m}_h C_p \Delta T_c \tag{17}$$

where C_p is the specific heat of air.

Based on the calculation results in this section, $H_{ice,max}$, η_{ave}, and Q_{loss} of the spinners before and after optimization were compared to quantitatively analyze and evaluate the optimization effect. The results are shown in Table 5. $H_{ice,max}$ decreased substantially in Cases 1–3 and 6, while Cases 4 and 5 remained ice-free before and after optimization. For Cases 1–3, $H_{ice,max}$ decreased by 22.37%, 52.87%, and 59.09%, respectively. For Case 6, $H_{ice,max}$ decreased from 1.64 mm before optimization to no ice accretion after optimization, representing a reduction of 100%. The improvement in η_{ave} was even more significant. η_{ave} increased from 0.27 to above 0.42. η_{ave} for Cases 1–6 increased by 54.45%, 55.74%, 54.45%, 68.01%, 66.84%, and 65.36%, respectively. Under Cases 1–6, the Q_{loss} decreased by 14.29%, 12.2%, 12.5%, 16.6%, 14.76%, and 13.27%, respectively. $H_{ice,max}$ is a parameter for evaluating the severity of local ice accretion. η_{ave} is a parameter for evaluating the overall ice accretion

amount on the spinner. Q_{loss} is a parameter for evaluating the energy consumption of the anti-icing system. The consistent reduction in Q_{loss} under all six operating conditions indicates that the optimized spinner requires less thermal energy from the compressor bleed air to achieve the required anti-icing performance. This reduces the demand for high-temperature compressor bleed air and, consequently, the energy consumption and engine performance penalty associated with the anti-icing system. By combining these key parameters, both the local ice accretion height and the overall ice accretion amount on the spinner surface can be assessed simultaneously, while the thermal-energy requirement of the anti-icing system can also be evaluated. The optimization results indicate that both $H_{ice,max}$ and η_{ave} of the optimized spinner were significantly improved, while Q_{loss} was consistently reduced under all six cases. This demonstrates that, compared with the spinner before optimization, the optimized spinner configuration obtained in this study effectively improves the anti-icing performance, reduces the icing risk, and decreases the thermal-energy demand on the compressor bleed-air system.

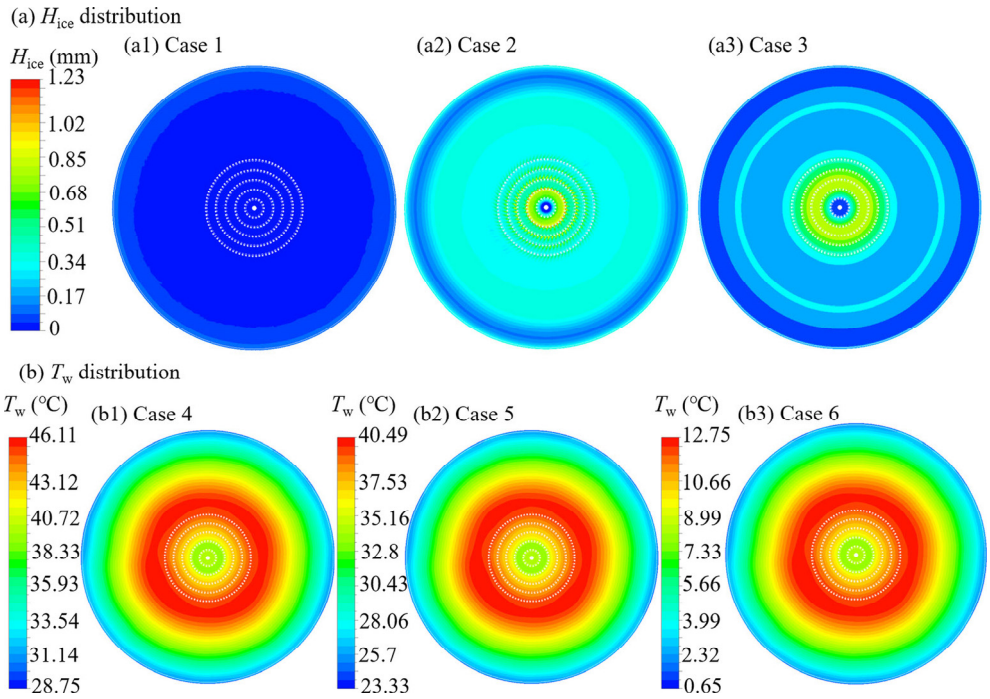

Figure 15. H_{ice} and T_w distributions of the optimized spinner.

The optimization in this study is limited to the effects of hole structure parameter variations on anti-icing performance under idle and maximum thrust conditions. Optimization of the hot air anti-icing spinner under different incoming flow conditions and icing conditions will be carried out in future research. The applicability of the present surrogate is limited to the spinner design family and parameter domain considered in this study. Specifically, the baseline spinner shape, dimensions, cone angle, hole row number, hole pattern, and leading-edge hole design were fixed, while only the row spacing A = 4–12 mm, column spacing B = 20–40 mm, and hole diameter C = 1–3 mm were varied. Therefore, the model should be regarded as an interpolation-based surrogate for optimizing these three parameters within the prescribed design space, rather than as a general predictor for arbitrary spinner geometries. Its direct application outside these ranges or to different spinner and hole layout designs is not supported by the present training data. Future work will expand the database to include additional geometric variables and spinner configurations.

Table 5. Comparison of anti-icing performance of the hot air anti-icing spinner under different icing conditions before and after optimization.

Case	1	2	3	4	5	6
$H_{ice,max}$ before optimization (mm)	0.76	2.61	1.98	no icing	no icing	1.64
$H_{ice,max}$ after optimization (mm)	0.59	1.23	0.81	no icing	no icing	no icing
η_{ave} before optimization	0.2753	0.2752	0.2751	0.2757	0.2771	0.28
η_{ave} after optimization	0.4252	0.4286	0.4249	0.4632	0.4623	0.463
Q_{loss} before optimization (kW)	0.42	0.41	0.4	7.89	7.79	5.05
Q_{loss} after optimization (kW)	0.36	0.36	0.35	6.58	6.64	4.38
Optimization margin of $H_{ice,max}$	22.37%	52.87%	59.09%	–	–	100%
Optimization margin of η_{ave}	54.45%	55.74%	54.45%	68.01%	66.84%	65.36%
Reduction magnitude of Q_{loss}	14.29%	12.2%	12.5%	16.6%	14.76%	13.27%

4. Conclusions

This study developed an integrated framework for the coordinated design of hole parameters in a rotating hot air anti-icing spinner. The framework combined orthogonal sampling, multi-physics icing simulations, a coupled neural network surrogate, and multi-objective genetic optimization. The main conclusions are summarized as follows:

(1) An $L_9(3^4)$ orthogonal array was used to coordinate hole parameters A, B, and C with only nine spinner configurations. These three parameters were jointly investigated by integrating the rotational force model, thermal–fluid–structural coupled model, and phase interface data exchange model. The resulting η, β, and H_{ice} fields revealed strong configuration dependence: η_{ave} varied from 0.1080 to 0.5988, β_{max} reached 0.2416, and $H_{ice,max}$ was 3.16 mm. Spinners 1, 2, and 4 remained ice-free at the leading edge, confirming the combined influence of hole arrangement, rotation, hot air film development, and droplet impingement.

(2) A dual-branch coupled neural network was established to simultaneously predict the pointwise H_{ice} and η distributions. The final model achieved R^2 = 0.9751 and RMSE = 0.04623 mm for H_{ice}, and R^2 = 0.8839 and RMSE = 0.06688 for η. Multi-objective optimization was then formulated by minimizing $H_{ice,max}$ and maximizing η_{ave}. In terms of $H_{ice,max}$ and η_{ave}, $(H_{ice,max})_{min}$, $(\eta_{ave})_{max}$, and knee-point solutions were (0.382 mm, 0.305), (1.994 mm, 0.592), and (0.863 mm, 0.451). The knee-point solution was selected as the optimal configuration. The Pareto front demonstrated that reducing cumulative local ice accretion can be accompanied by an increased extreme local thickness risk, thereby quantifying the competition between the two objectives.

(3) The optimized configuration, A = 4.7187 mm, B = 22.7646 mm, and C = 2.0639 mm, was re-evaluated under idle and maximum icing conditions. For Cases 1–3, $H_{ice,max}$ decreased by 22.37%, 52.87%, and 59.09%; Cases 4 and 5 remained ice-free, while Case 6 changed from $H_{ice,max}$ = 1.64 mm to no icing. Meanwhile, η_{ave} increased by 54.45–68.01% across all conditions (from approximately 0.27 to above 0.42), and Q_{loss} decreased by 12.2–16.6%. The reduction in Q_{loss} indicates that the optimized spinner requires less thermal energy from the compressor bleed air. The optimization in this study has only been validated through numerical simulation. The results show that the anti-icing performance of the optimized spinner has been significantly improved. However, icing wind tunnel tests for the optimized spinner have not yet been conducted. Therefore, the combined improvements in $H_{ice,max}$, η_{ave}, and Q_{loss} demonstrate that the optimized hole configuration simultaneously reduces local icing risk, improves overall surface heating performance, and decreases the energy demand of the hot air anti-icing system.

This study conducted the optimization of hole structures for a hot air anti-icing spinner. However, due to limitations in computational resources and experimental conditions, the

sample size used in this study was limited. Training relied heavily on existing CFD data, the extrapolation capability of the model was relatively weak, and experimental validation of the optimized configuration was not performed. These limitations will be addressed in future research.

Author Contributions: Conceptualization, W.D. and Z.L.; methodology, L.W.; software, B.Q.; formal analysis, Y.L.; resources, X.G. and H.L.; writing—original draft preparation, W.D.; writing—review and editing, Y.X.; visualization, T.H. All authors have read and agreed to the published version of the manuscript.

Funding: This research was funded by the National Natural Science Foundation of China (grant number 52206066), the National Key Research and Development Program of China (grant number 2025YFE0200300), the Taihang National Laboratory Project (grant number B7023), and the Beijing Natural Science Foundation (grant number L2608008).

Data Availability Statement: The data of this article will be made available upon request.

Conflicts of Interest: Author 4 (Zhaoqi Liu) is currently employed by Contemporary Amperex Technology Co., Ltd. (CATL). The research reported in this paper was conducted during his master's studies at Beihang University, prior to his employment at CATL. CATL provided no financial support, technical resources, or data for this study, and had no role in the design of the study; in the collection, analyses, or interpretation of data; in the writing of the manuscript; or in the decision to publish the results. The other authors declare no conflicts of interest. No potential commercial interests are identified beyond the disclosed employment relationship.

References

1. Nohooji, S.G.; Tembely, M. Analysis of Electro-Thermal De-Icing on a NACA0012 Airfoil Under Harsh SLD Conditions and Different Angles of Attack. *Aerospace* **2025**, *12*, 883. [CrossRef]
2. Dong, Z.Y.; Zheng, H.R.; Yan, H.; Wang, P.Y.; Dong, W. Swirl-jet coupled flow and heat transfer in aircraft nacelle anti-icing D-duct. *Aerosp. Sci. Technol.* **2026**, *178*, 113233. [CrossRef]
3. Ray, R.; Raj, L.P.; Jo, J.H.; Cho, M.Y.; Kwean, J.W.; Myong, R.S. Multiphysics anti-icing simulation of a CFRP composite wing structure embedded with thin etched-foil electrothermal heating films in glaze ice conditions. *Compos. Struct.* **2021**, *276*, 114441. [CrossRef]
4. Veerakumar, R.; Hu, H.Y.; Tian, L.C.; Han, N.H.; Hu, H. An experimental study of rime ice accretion on bundled conductors. *Exp. Therm. Fluid Sci.* **2023**, *147*, 110962. [CrossRef]
5. Gao, X.; Deng, W.H.; Liu, Z.Q.; Chen, S.G.; Wang, P.F.; Qiu, B.R.; Xia, Y.K.; Li, H.W. Icing dynamics on the rotating spinners of aero-engines. *Int. J. Heat Mass Transf.* **2026**, *263*, 128627. [CrossRef]
6. Wei, Z.J.; Li, C.; Ren, G.M.; Gan, X.H. Fully-coupled modeling and analysis of the influence of anti-icing bleed air system of engine inlet duct on compressor performance. *Case Stud. Therm. Eng.* **2024**, *54*, 104013. [CrossRef]
7. Hu, Y.P.; Du, Y.X.; Zheng, W.L.; Chen, W.J.; Jiang, Y.T.; Qiu, C.B. Study of hot air anti-icing and water film distribution on an aeroengine strut. *Case Stud. Therm. Eng.* **2026**, *82*, 108097. [CrossRef]
8. Li, L.K.; Liu, Y.; Tian, L.C.; Hu, H.Y.; Hu, H.; Liu, X.J.; Hogate, I.; Kohli, A. An experimental study on a hot air-based anti-/de-icing system for aero-engine inlet guide vanes. *Appl. Therm. Eng.* **2020**, *164*, 114778. [CrossRef]
9. Zheng, G.J.; Tan, H.J.; Wu, Z.L.; Luo, G.; Xu, T.Z. Ingestion characteristics of ice slab shed from the lip of a branched turboprop inlet. *Chin. J. Aeronaut.* **2026**, *39*, 103791. [CrossRef]
10. Tian, L.C.; Hu, H.Y.; Veerakumar, R.; Hu, H. Ice accretion characteristics on rotating aeroengine fan blades. *Exp. Therm. Fluid Sci.* **2024**, *155*, 111181. [CrossRef]
11. Zheng, H.R.; Zhang, Z.L.; Dong, Z.Y.; Dong, W. An integrated model for prediction of ice crystal icing and compressor performance degradation in a three-stage axial compressor. *Aerosp. Sci. Technol.* **2026**, *178*, 112394. [CrossRef]
12. Tetteh, E.; Loth, E.; Neuteboom, M.O.; Fisher, J. In-flight gas turbine engine icing: Review. *AIAA J.* **2022**, *60*, 5610–5632. [CrossRef]
13. Yoon, W.; Kim, J.; Chung, C.; Park, J. Numerical study on prediction of icing phenomena in intake system of diesel engine: Operating conditions with low-to-middle velocity of inlet air. *Energy* **2022**, *248*, 123569. [CrossRef]
14. Hu, Y.P.; Zheng, W.L.; Wu, C.; Fan, Y.X.; Du, Y.X.; Yuan, H.R.; Zhang, T.Y.; Jing, S.L. Investigation of impingement-film composite anti-icing on a rotating spinner. *Aerosp. Sci. Technol.* **2026**, *174*, 111878. [CrossRef]

15. Yang, Q.; Guo, X.F.; Zheng, H.R.; Dong, W. Single- and multi-objective optimization of an aircraft hot air anti-icing system based on reduced order method. *Appl. Therm. Eng.* **2023**, *219*, 119543. [CrossRef]
16. Liu, Y.; Qu, J.G.; Yi, X.; Wang, Q. A Monte Carlo Lagrangian droplet solver with backpropagation neural network for aircraft icing simulation. *Trans. Nanjing Univ. Aeronaut. Astronaut.* **2023**, *40*, 566–577. [CrossRef]
17. Wittig, J.; Tzortzinis, G.; Modler, N.; Lissner, M.; Filippatos, A. Vibration-based ice monitoring of composite blades using artificial neural networks under different icing conditions. *Cold Reg. Sci. Technol.* **2025**, *231*, 104379. [CrossRef]
18. Ogretim, E.; Huebsch, W.; Shinn, A. Aircraft ice accretion prediction based on neural networks. *J. Aircr.* **2006**, *43*, 233–240. [CrossRef]
19. Chang, S.N.; Leng, M.Y.; Wu, H.W.; Thompson, J. Aircraft ice accretion prediction using neural network and wavelet packet transform. *Aircr. Eng. Aerosp. Technol.* **2016**, *88*, 128–136. [CrossRef]
20. Suo, W.; Sun, X.X.; Zhang, W.; Yi, X. Aircraft ice accretion prediction based on geometrical constraints enhancement neural networks. *Int. J. Numer. Methods Heat Fluid Flow* **2024**, *34*, 3542–3568. [CrossRef]
21. Li, F.Y.; Cui, H.M.; Su, H.J.; Iderchuluun; Ma, Z.P.; Zhu, Y.X.; Zhang, Y. Icing condition prediction of wind turbine blade by using artificial neural network based on modal frequency. *Cold Reg. Sci. Technol.* **2022**, *194*, 103467. [CrossRef]
22. Li, T.S.; Xu, J.H.; Liu, Z.S.; Wang, D.D.; Tan, W. Detecting icing on the blades of a wind turbine using a deep neural network. *Comput. Model. Eng. Sci.* **2023**, *134*, 767–782. [CrossRef]
23. Kallarappayi, A.; Nixon, J.D.; Bégin-Drolet, A.; Godreau, C. Machine- and deep-learning models for wind turbine icing prediction across multiple horizons: The influence of ice sensors and weather forecasts. *Cold Reg. Sci. Technol.* **2026**, *248*, 104940. [CrossRef]
24. Cardona, A.; Nakouri, H.; Brassard, J.-D.; Momen, G. Machine learning prediction of aircraft anti-icing fluid endurance: A comparative study using natural and artificial snow data. *Aerosp. Sci. Technol.* **2026**, *176*, 112103. [CrossRef]
25. Mirjalili, S.; Saremi, S.; Mirjalili, S.M.; Coelho, L.S. Multi-objective grey wolf optimizer: A novel algorithm for multi-criterion optimization. *Expert Syst. Appl.* **2016**, *47*, 106–119. [CrossRef]
26. Ma, H.P.; Zhang, Y.J.; Sun, S.Y.; Liu, T.; Shan, Y. A comprehensive survey on NSGA-II for multi-objective optimization and applications. *Artif. Intell. Rev.* **2023**, *56*, 15217–15270. [CrossRef]
27. Yu, D.K.; Xu, Z.W.; Mei, M. Multi-objective task scheduling optimization based on improved bat algorithm in cloud computing environment. *Int. J. Adv. Comput. Sci. Appl.* **2023**, *14*, 1091–1100. [CrossRef]
28. Faroqi, H. Multiobjective route finding in a multimode transportation network by NSGA-II. *J. Eng. Appl. Sci.* **2024**, *71*, 81. [CrossRef]
29. Zuo, F.Y.; Ma, L.J.; Wang, S.Q.; Pirozzoli, S. Suppression separation in conical shock wave/turbulent boundary layer interactions through porous bleed control. *Propuls. Power Res.* **2026**, *15*, 1–15. [CrossRef]
30. Gao, X.; Qiu, B.R.; Wang, Z.J.; Li, H.W. Influence of spinner shape on droplet impact over rotating spinners. *Aerospace* **2023**, *10*, 68. [CrossRef]
31. Umana, M.E.; Li, H.; Yang, X.F.; Uglanov, D.A.; Kedam, N. A comparative study of liquid film cooling on a flat plate using SPH and VOF methods. *Aerospace* **2026**, *13*, 70. [CrossRef]
32. Wang, Y.Y.; Jiang, X.L.; Wang, L.H.; Cui, R.F.; Chen, P.Y.; Wang, X. Numerical simulation of supercooled droplet impact with a velocity-gated Darcy source. *Aerospace* **2025**, *12*, 902. [CrossRef]
33. Gao, X.; Deng, W.H.; Liu, S.; Chen, S.G.; Li, H.W. Study on icing multiphase heat transfer process based on phase interface data exchange. *J. Aerosp. Power* **2023**, *38*, 1561–1570. [CrossRef]
34. Deng, W.H.; Chen, S.G.; Wang, L.C.; Qiu, B.R.; Ye, J.D.; Xia, Y.K.; Khezzar, L.; Li, H.W.; Gao, X. Heat transfer characteristics and multi-parameter evaluation of hot air anti-icing performance on a rotating aero-engine spinner. *Appl. Therm. Eng.* **2026**, *305*, 133013. [CrossRef]
35. Hisam, M.W.; Dar, A.A.; Elrasheed, M.O.; Khan, M.S.; Gera, R.; Azad, I. The versatility of the Taguchi method: Optimizing experiments across diverse disciplines. *J. Stat. Theory Appl.* **2024**, *23*, 365–389. [CrossRef]
36. Mole, A.; Skillen, A.; Revell, A. Multi-fidelity surrogate modelling of wall mounted cubes. *Flow Turbul. Combust.* **2023**, *110*, 835–853. [CrossRef]
37. Sullivan, J.; Mirhashemi, A.; Lee, J. Deep learning-based inverse design of microstructured materials for optical optimization and thermal radiation control. *Sci. Rep.* **2023**, *13*, 7382. [CrossRef] [PubMed]
38. Sato, H.; Igarashi, H. Fast multi-objective optimization of electromagnetic devices using adaptive neural network surrogate model. *IEEE Trans. Magn.* **2022**, *58*, 8202209. [CrossRef]
39. Shi, Q.L.; Wang, H.; Cheng, H.; Cheng, F.; Wang, M.L. An adaptive sequential sampling strategy-based multi-objective optimization of aerodynamic configuration for a tandem-wing UAV via a surrogate model. *IEEE Access* **2021**, *9*, 164131–164147. [CrossRef]

40. Neeharika, M.S.; Shobhana, V.; Katal, N. Multi-objective optimal synthesis of robust control systems for plants exhibiting non-minimum phase and integrating behaviour. *Sci. Rep.* **2025**, *15*, 40712. [CrossRef] [PubMed]
41. Deng, W.H.; Qiu, B.R.; Tao, J.N.; Li, H.W.; Chen, S.G.; Wang, P.F.; Guan, Q.S.; Ma, L.; Xia, Y.K.; Gao, X. Analysis of anti-icing characteristics for rotating spinners with hot air film. *Propuls. Power Res.* **2026**, *15*, 669–688. [CrossRef]

Disclaimer/Publisher's Note: The statements, opinions and data contained in all publications are solely those of the individual author(s) and contributor(s) and not of MDPI and/or the editor(s). MDPI and/or the editor(s) disclaim responsibility for any injury to people or property resulting from any ideas, methods, instructions or products referred to in the content.